A fast and portable imager for neutron and gamma emitting radionuclides

Hajir Al Hamrashdi [1,a,b], David Cheneler [a] and Stephen D. Monk [a]

[a] Engineering department, Lancaster University, Lancaster, LA1 4YW.

[b] Physics Department, Sultan Qaboos University, Muscat, Oman, 123.

ABSTRACT

Here a novel, real-time, highly-compact imaging system capable of detecting and localising gamma rays, thermal and fast neutrons is reported. The imaging system presented in this research comprises of a front-end containing three detection layers with a unique combination of scintillators optimised for multi-particle detection, and backed with silicon photomultiplier diode arrays to enable source localisation and to maximise efficiency. The system exploits Compton and neutron scattering techniques simultaneously to constitute a dual-mode radiation camera. Application-specific software algorithms are implemented here to process the numerous signals from the system and to reconstruct the location of radioactive sources using a back-projection technique. The three front-end detection layers fit within a volume of 120 mm × 120 mm × 200 mm, offering a uniquely compact imaging solution. A prototype of the instrument and the associated electronics have been designed using Monte Carlo simulations, and tested with Cs-137 (given its singular gamma-ray component) and Cf-252 (for its mixed neutron and gamma-ray emission). Experimental results indicate that the system can detect and localise both gamma-ray and neutron sources successfully, with intrinsic efficiencies in the order of 10^{-4}. All results have been achieved within a scan time of 60 seconds and with a further data processing time of less than 60 seconds, for gamma sources of ~300 kBq and neutron sources of 10^6 neutrons per second (total) in close proximity (< 300 mm). Whilst high-speed, mixed-field, particle-imaging systems have numerous applications within both nuclear and non-nuclear fields; this particular system has been optimised for use within the areas of nuclear materials assay and proliferation prevention.

Keywords: Gamma rays, neutrons; detection; Compton scattering; neutron scattering; real-time imaging; proliferation prevention.

1   Introduction

Global imperatives to decarbonise electricity supplies have resulted in a variety of new nuclear build programmes and related developments in nuclear fuel technology. These developments have the potential to generate new challenges at national and international levels [1, 2]. The diversion of nuclear materials deemed unlawful under international regulations might involve several different stages, starting with for example: the acquisition of safeguarded material, its transportation and eventual deposition at a point where non-peaceful use might be the intent and concern. Of key strategic importance in this regard is the deployment of detection technologies capable of identifying and tracking special nuclear materials at national and international cross points, ports and borders [3, 4]. These areas can be either controlled (e.g., associated with secure areas within airports, border and cargo inspection points etc.) or uncontrolled (e.g., at airport terminals, train stations and so forth). The latter scenario is associated typically with a complex environment where innovative detection technologies are required [4]. In particular, these technologies usually need to be mobile (so they can be placed as required and offer flexibility when closer inspection is required) and offer fast data acquisition times (to ensure that the materials in question can be identified rapidly and tracked within what can be dynamic environments).

---

[1] Corresponding author.

E-mail: h.alhamrashdi@lancaster.ac.uk or hajir@squ.edu.om

General radiation cameras have been utilised widely as thoroughly reviewed by H. Al Hamrashdi et al. [4], with some systems finding industrial designation such as RadCam [5] GAMPIX [6-8], GeGi [9] and Cartogam [10]. Systems that detect gamma rays and neutrons both passively and simultaneously are widely described and utilised within the literature [4, 11-15]. Such multi-mode systems possess an obvious advantage over single particle detection for security applications as it permits the location of a wider range of radioactive and nuclear materials. Compton and neutron scattering are physical interaction phenomena that are well-established, with Compton scattering being especially popular in the medical industry [16-18] and possessing intrinsic detection efficiencies typically between 10^{-6} to 10^{-3} [19, 20]. The concept of combining neutron and Compton scattering techniques to detect fast neutrons and gamma rays in safeguarding applications was first suggested by Polack et al. [21] in 2011 and experimentally investigated by Poitrasson-Riviere et al. in 2014 [22]. The system described by Poitrasson-Riviere et al. consists of three detection arrays, each with sixteen, relatively large EJ-309 and NaI(Tl) scintillation detectors, and offer comparable detection and localisation abilities to standard multilayer designs. Designed as a lab-based proof-of-concept study, the configuration is not practical for many security applications due to the sheer bulk of the system. This paper describes the design, construction and testing of a portable and real-time, compact neutron and gamma-ray detection and imaging instrument, along with the assessment of its detection abilities and characteristics. The main features of this design are:

- The prototype front-end is highly compact, having dimensions of 200 mm x 120 mm x 120 mm and a mass of 3 kg. When battery powered, this allows the instrument to be utilised at any stage during the monitoring protocols of radioactive and nuclear materials at national and international cross points, ports and borders.
- The design targets gamma rays in the Compton energy range (~10 keV to ~10 MeV), thermal and fast neutrons, and is capable of simultaneous detection of all three.
- The instrument features fast data acquisition techniques leading to a 60-second scan time, short compared to most other imaging cameras. This allows rapid creation of a source position probability map that can be used to identify potential radiological sources. (The scan time is achieved for gamma sources of ~300 kBq and neutron sources of 10^6 neutrons per second (total) in close proximity < 300 mm).

The main target application for this system is border security, although it is anticipated that a more mature version of the design could be applied within alternative fields such as medical and industrial imaging. Previous work by the authors [23, 24] concerned the determination of aspects such as the materials used in the front end of the instrument and the optimal distances between layers. The work described here describes the physical construction of the front end, the electronics used in the instrument and the software utilised to extract and present the data generated. For reasons of brevity, the development of Pulse Shape Discrimination (PSD) techniques to be used with this instrument are to be discussed in future work.

2   Imaging Concept

Within this imaging system, Compton scattering is exploited to detect gamma rays with energies of between ~10 keV and ~10 MeV [25]. Similarly, neutron scattering technology is used here to detect fast neutrons with energies higher than 1 keV, with additional capture technologies also integrated to detect low-energy neutrons; the detection system is shown Figure 1. Each of the four scintillators used have an active detection area of 27 mm × 27 mm. The materials selected and the particular thicknesses used are the result of an earlier, in-depth Monte Carlo-based optimisation study by the authors [23].
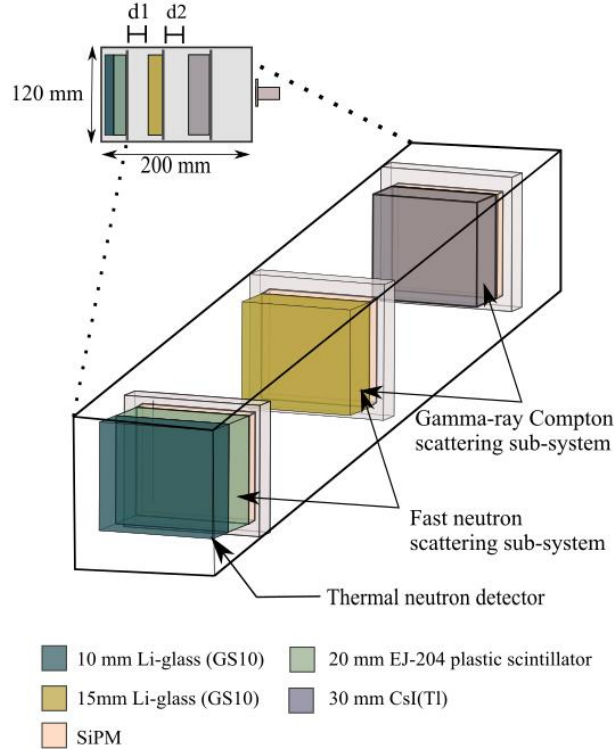
Figure 1: A schematic of the imaging system comprising of scintillator and silicon photomultipliers (SiPMs). The upper diagram representing a side elevation of the system and the lower diagram representation a front elevation of the system. Here, d1 and d2 in the side elevation view are the separation distances between layers. The values of d1 and d2 were both 30 mm.

The three layers are constructed from a unique combination of scintillators optimised for multi-particle detection. Each of the layers is backed by a segmented (8×8 array) silicon-based photomultiplier (SiPM), and a compact, photon-counting transducer device that is used to localise and quantify photons produced in the scintillation layers, as described below:

- The first layer consists of two detectors coupled via optical gel. The first is a 10 mm thick, natural lithium glass scintillator (i.e. 6.6% of the lithium content is Li-6; GS10 from Scintacor Ltd., Cambridge, UK [26]) which captures thermal neutrons, whilst it is anticipated that fast neutrons and gamma rays generally pass through without interaction. The second is a 20 mm thick EJ-204 plastic scintillator (Eljen Technology, Sweetwater, TX, USA) [27]) that serves as the fast neutron scattering media within the neutron-scattering sub-system, again without significantly affecting the gamma-ray flux. This particular thickness of lithium glass detector in this layer has been selected to optimise thermal neutron detection while minimising gamma-ray interaction probability in the detector [23].

- The second layer comprises a 15-mm thick lithium glass scintillator (GS10 from Scintacor Ltd. as in the first layer) which captures the neutrons scattered and thermalized by the plastic scintillator in the first layer. The same crystal serves as the first Compton scattering layer in the Compton scattering sub-system.

- The third layer is a 30 mm thick thallium-doped, caesium iodide (CsI(Tl)) scintillator (John Caunt Scientific Ltd., UK [28]) which forms the final gamma-ray detection layer in the Compton scattering sub-system.

The lithium glass used in the imaging system is a cerium-activated, silicate glass with lithium content in its natural isotopic abundance. As shown in the previously-mentioned material characteristics optimisation study (Al Hamrashdi et al. [23]), the GS10 lithium glass exhibits superior scattering capabilities compared to other scintillation materials that are sensitive to both neutrons and gamma rays. EJ-204 is a general-purpose, plastic scintillator which possesses a 1.1 H:C ratio and demonstrates sensitivity to both fast neutrons and photons with energy of less than 100 keV. Indeed, EJ-204 (also known as NE-104 and BC-404) possesses one of the highest scintillation efficiencies amongst all plastic detectors with 10,400 photons generated per MeV of incident

electrons. CsI(Tl) is a widely-utilised, inorganic scintillator renowned for its larger gamma-ray absorption coefficient compared to sodium iodide and a higher absolute light yield of 65,000 photons/MeV compared to 38,000 photons/MeV for NaI(Tl) [25].

Thermal neutron detection is achieved in the first lithium glass layer via the ^{6}Li(n,α)^{3}H thermal neutron capture reaction. The alpha and triton products of this reaction are highly ionising, with energies of 2.73 MeV and 2.05 MeV respectively [25], and transfer their energy to the cerium-activated lithium glass. Pulses generated in this layer are of consistent height and shape characteristics albeit with slight variations due discrepancies in photon transport and photodetector response. Fast neutron detection is the result of neutrons undergoing elastic scattering whilst interacting with the protons within the EJ-204 plastic scintillator located in the first layer, followed by the detection of the scattered neutrons in the second layer. The scattered protons in the EJ-204 deposit most of their energy within this volume (the range of a 10 MeV proton in general PVT plastic scintillators is c.a. 1.2 mm [29]) generating visible photons, which are detected by a SiPM. Within the second layer of the system, some of the lower energy scattered neutrons will interact with the lithium glass through capture reactions or elastic scattering, with both reactions producing visible photons. The pulses generated from these interactions are utilised to measure the time-of-flight (TOF) of the neutrons between the two layers. Figure 2 shows a schematic of the components used in the neutron-scattering technique, and the parameters used in the analysis.
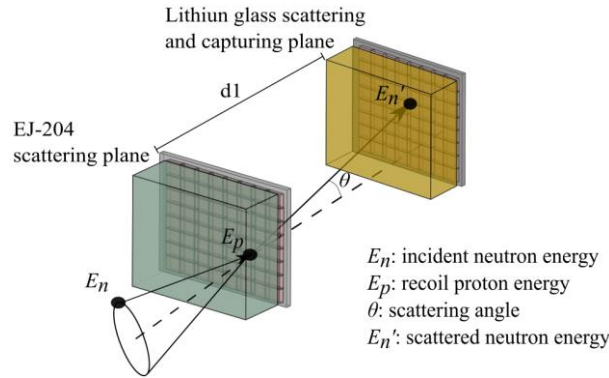

Figure 2: A schematic of the neutron scattering sub-system components. The schematic illustrates a successful neutron scattering event within the system in which the neutron will first interact in EJ-204 detector, producing a proton that will eventually generate scintillation photons in the scintillator. The scintillation photons will then be collected in the SiPM of that layer. The scattered neutron then interacts in the lithium glass layer. Secondary particles from this interaction will then generate scintillation photons that will be collected in the SiPM of that layer.

The scattering angles and incident trajectories can be calculated from the relative positions of the detected pulses via the position of activated pixels in the SiPM. The energy of an incident neutron is assumed to be the sum of the energy of the scattered proton, E_p, and of the energy of the scattered neutron, E'_n [30, 31]. These energies are related to the scattering angle, θ, through equation 1:

$$\tan^2\theta = E_p/E'_n \tag{1}$$

The energy of the scattered neutron can be calculated using the time-of-flight (TOF) measurement between the two SiPMs, as shown in equation 2.

$$E'_n = 0.5\, m_n\, (d1^2/TOF^2) \tag{2}$$

Where d1 is the separation distance between the two SiPM arrays, and m_n is the mass of a neutron. The probable origin of the neutron source is formed by creating probability cones coincident on the plane defined by the scattering angle. The compound images of the intersection areas of all of the resultant ellipses can then be used to estimate the most likely location of the incident neutron source.

The Compton detection technique is used here to overcome the drawbacks of conventional physical collimation, the most significant of which concerns the narrow range of incidence angle, which has a direct effect on detection efficiency [16, 17]. Two layers of scintillator are utilised in this Compton scattering subsystem: the second lithium glass scintillator operating as the photon-scattering layer with the CsI(Tl) scintillator operating as the photon detection layer. The scattering angles and incident trajectories can be related using conservation of energy and conservation of momentum equations as shown in equation 3 and Figure 3. It is assumed that the energy of the incident gamma-ray photon is the sum of the measured energy of the recoil electron E_e and the measured, absorbed, scattering photon energy $E'\gamma$.
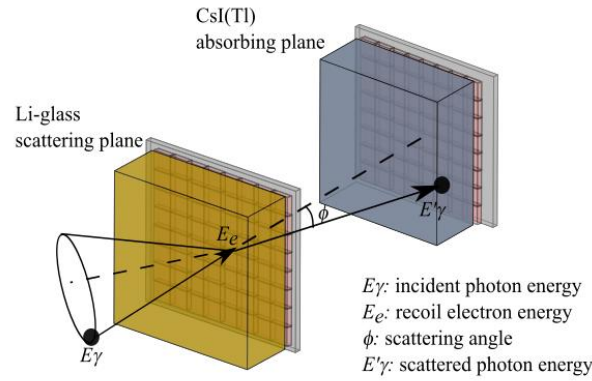

Figure 3: gamma particle collides with an atom in the lithium glass via the Compton Effect, the electron producing visible photons in the volume, which are collected in the SiPM. The photon scattered in this volume then enters the CsI(Tl) scintillator with the electron produced via the photoelectric effect producing visible photons which are collected in the associated SiPM.

$$\cos\phi = 1 - mc^2 \left[\left(\frac{1}{E'\gamma} \right) - \left(\frac{1}{E'\gamma + E_e} \right) \right] \tag{3}$$

Where m is rest mass of an electron and c is the speed of light.

The high fill-factor J-series SiPM sensor array (ArrayJ-30035-64P-PCB 8x8 SiPM, SensL, Cork, Ireland [28]) is used as the photodetector within each of the three detection layers of the design described in this paper. The typical breakdown voltage (V_{br}) of this particular array is 24.5 V, with a sensitive spectral range of between 200 nm and 900 nm; a limit that comfortably spans the wavelength of maximum emission for lithium glass (395 nm), EJ-204 (408 nm) and CsI(Tl) (550 nm) [25]. The main features of the J-series SiPM array are the low dark count rate (typically 50 kHz/mm^2 at 2.5V above V_{br} and 80 kHz/mm^2 at 5V above V_{br}) and the high photon detection efficiency (38% at 2.5V above V_{br} and 51% at 5V above V_{br}). The photon detection efficiency extends into the blue range of the electromagnetic spectrum, matching the wavelength range of the lithium glass and EJ-204 emission spectra [32]. This latter feature contributes directly to the reduction of dark current as the penetration of light in the blue region is shallow in a silicon wafer, minimising the depth of the generated electric field and subsequent spontaneous generation of electrons [25]. The main physical feature of the ArrayJ-30035-64P-PCB 8x8 SiPM is the efficient use of space within the active area of the array. The arrays used here feature 64 individual pixels (each with a total number of 5,676 SPAD microcells) with each pixel featuring a pitch of 3.16 mm equating to a total size of 26.68 mm × 26.68 mm, offering high-resolution 2D-mapping of incident and locally-generated pulses [32].

3   Experimental Set-up

The experimental system consists of three 'zones'. The measurement zone features the three-layer detectors assembly as described above, the front-end electronics associated with the detection layers, and the three power supplies that provide the 29.4 V DC required by the SiPMs. The 192 channels of data generated in this zone are fed into the readout circuit zone, which comprises of a large volume of bespoke electronics designed to process

the data from the SiPM pixels and utilising a ±12 V, 10 A power supply. Finally, the control zone incorporates the software used to collect and process the data produced by the instrument.

3.1 Measurement Zone

The scintillator detectors are orientated vertically in a stainless steel enclosure with a wall thickness of 4 mm to simultaneously reduce the influence of background radiation while offering structural integrity and machinability. The enclosure has external dimensions of 120 mm × 120 mm × 200 mm, reflecting the small form factor of the imaging system. The 8×8 SiPM arrays are placed in optical contact with the scintillators within each layer, and are mounted on ARRAYJ-BOB3-64P (SensL) breakout boards. Each SiPM pixel has a dedicated simple current-to-voltage converter consisting of a 47 Ω resistor in series with the diode. Off-the-shelf benchtop power supplies were used to provide 29.4 V of reverse bias, which was applied across the resistor and diode, with the output, read across the diode and transmitted via ribbon cable to the readout circuit. Figure 4 shows the SiPM array with the front-end electronics.
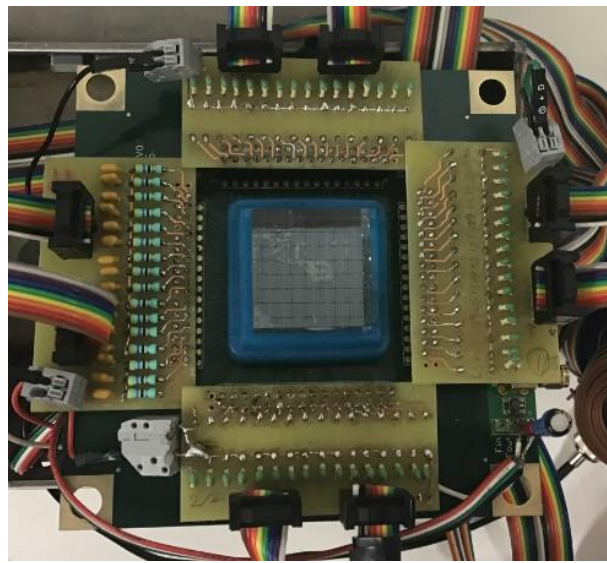

Figure 4: A photograph of the SiPM array with the front-end electronics used in this research.

The characteristic equation describing an output current pulse from the SiPM has been discussed previously by A. Spinelli and A. L. Lacaita [33], and by R. Turchetta [34]. The shape of the raw pulses from a single SPAD (or microcell) is commonly described as a Dirac's delta pulse ($Q\delta(t-c)$). The total charge Q generated by each SPAD in the SiPM array being equal to $\Delta V(C_q+C_d)$; where ΔV is the overvoltage, C_q is the quenching capacitor value and C_d is the depletion region capacitance in the SiPM cell. The anode-cathode (standard) output of the SiPM module used in this design has a total capacitance of 1000 pF. Figure 5 showcases the processed and normalised output pulses from the SiPM when lithium glass, EJ-204 and CsI(Tl) detectors are utilised. The data were acquired using Agilent 54845A Infinium Oscilloscope with a sampling speed of 8 GSa/s and bandwidth of 1.5 GHz.
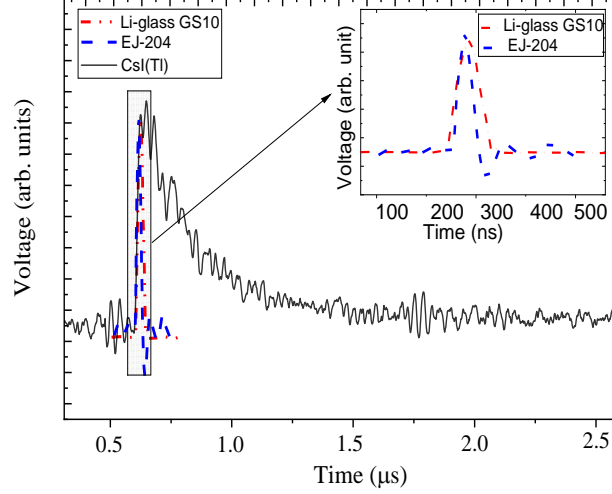
Figure 5: Pulses generated from an SiPM and front-end electronics (current-to-voltage converter) for lithium glass, EJ-204 and CsI(Tl) detectors, using a Cf-252 source (the inset figure is an enlarged proportion of the figure comprising close-ups of the lithium glass and EJ-204 short pulses).

Table 1 provides a list of the average rise and fall times of the three types of pulse featured in Figure 5. The rise time in the table refers to the time required for the leading edge of the pulse to rise from 10% to 90% of its maximum value, whereas fall time is the time required for the decaying edge of the pulse to fall from 90% to 10%.

Table 1: Rise time and fall time of SiPMs pulses for lithium glass, CsI(Tl) and EJ-204 (Note that measurements here are limited by the sampling speed of the oscilloscope utilised in this part of the experiment)

Detector	Maximum emission wavelength (nm)	Radiation source	Average rise time (ns)		Average fall time (ns)	
			Measured	Reported	Measured	Reported
Lithium glass	395	mixed	50.4 ± 0.9	NA	70 ± 3	70[1]
CsI(Tl)	550	gamma-ray	67 ± 2	NA	1600 ± 30	600 (fast component) /3340 (slow component)
EJ-204	408	mixed	NA	0.7[2]	NA	1.8[2]

[1] van Ejik et. al, 2012[35]
[2] https://eljentechnology.com/images/products/data_sheets/EJ-200_EJ-204_EJ-208_EJ-212.pdf [27]

EJ-204 is an appropriate scintillator choice within counting applications that require a fast response, as the material boasts a pulse rise and fall time of less than 3 ns and a pulse width at FWHM of 2.2 ns. While this is of great advantage in the TOF measurements, an issue occurs when sampling the pulse with conventional instrumentation, such as the oscilloscope. The high sampling speed of the Agilent 54845A Infiniium Oscilloscope allows the digitising of EJ-204 pulses and hence the plotting of the pulses shown in Figure 5, although the low input impedance (1 MΩ) can cause the undershooting observed in the EJ-204 pulse, which might affect further analysis on pulse shape discrimination.

3.2   Readout circuit zone

An application-specific readout circuit (ASRC) was designed in order to process each of the 192 pixels from the three SiPM arrays individually. There are three main levels of circuitry within the ASRC: (i) filtering and amplification, (ii) pulse comparison, and (iii) time-of-flight (TOF) measurement. The DAQ used here was the USB-2633 (Measurement Computing Corporation, USA) [36] which operates at a sampling rate of 1 MSa/s with

64 single-ended analogue inputs (1 GΩ input impedance) and three 8-bit digital inputs. Figure 6 shows a block diagram of the readout circuit with an example of the different stages in the ASRC for two channels. It should be noted that whilst this also features the current-to-voltage stage for completeness, this component is physically in the measurement zone as opposed to being in the application-specific readout circuit zone.
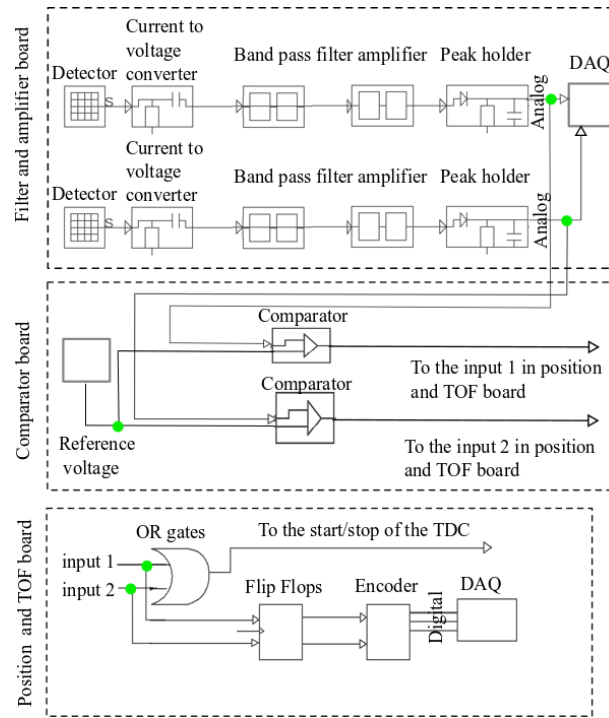

Figure 6: Block diagram of the ASRC showing, as an example, the transition of pulses within two of the channels.

The function of the first stage of the circuit is to filter and amplify the voltage pulses from each of the SiPM pixels via a high-pass filter and two inverting amplifiers (also acting as active low-pass filters). This features a cut off frequency of 10 GHz and a gain of 100 (Figure 7). The amplifier used is the low-noise and high-speed LT1226 (Linear Technology, USA) which features a gain bandwidth product of 1 GHz at ±12 V and slew rate of 400 V/ms.
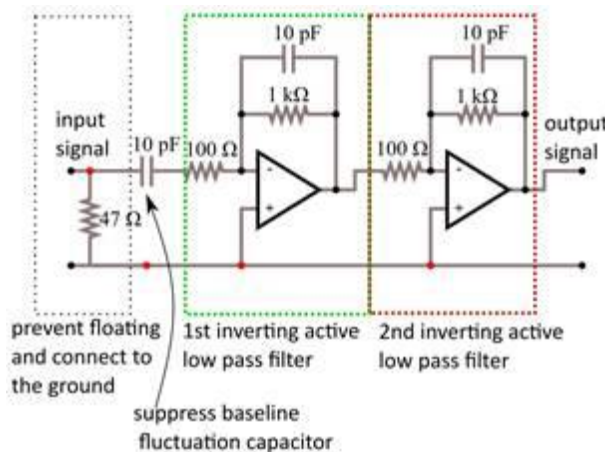

Figure 7: Schematic diagram of the double-inverting amplifier, active low-pass filters in the filter and amplifier boards.

An input pulse to this circuit, with a peak height of 80 mV and decay time of 1.6 µs, was found to correspond to an output pulse with a peak height of 5000 mV and a decay time of 200 µs. This allows for a longer time for digitisation and analysis of the signal as well as reducing the likelihood of pulses being lost while being read in

the DAQ. Each of these processed signals are input to a LM319MX dual high-speed comparator (Texas Instruments, USA [37] , where the peak amplitude of the pulse is compared to a user-adjustable reference voltage, which is set above the electrical noise and background levels. When the input voltage is above this reference threshold, it is treated as an 'event'. For each layer in the imaging system, there is a PCB featuring 32 LM319MX dual comparators (±12 V) which can compare 64 analog signals, simultaneously, in 80 ns. The output is sent to a voltage divider, comprising two 10-kΩ resistors (shown in Figure 8), resulting in a 'high' output pulse of 6 V.
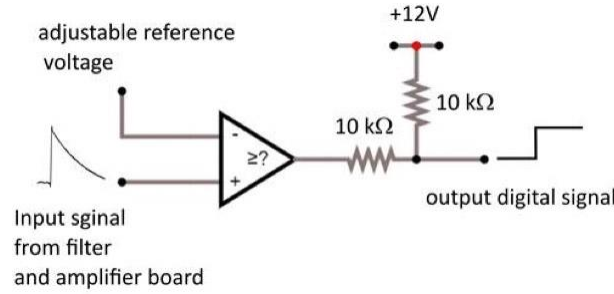

Figure 8: Main building block circuit for the comparator PCB.

These digital signals are then sent to the TOF circuit, which generates digital pulses to trigger a time-to-digital Converter (TDC) module via the start/stop input. The TOF circuit uses a series of rising-edge, trigger logic OR gates which determine whether any of the outputs from the comparators are non-zero at time 't'. This output is sent to the TDC7200EVM (Texas Instruments) evaluation module (used to operate and evaluate the TDC7200 TDC) to trigger the start/stop clock. This module possesses an input measurement range of between 12 ns and 500 ns, with a resolution of 30 ps - a range that roughly matches that of the scattered neutron TOF anticipated in these experiments. Within the measurement range of the TDC7200EVM (12 ns to 500 ns) and the separation distance between layers 1 and 2 (30 mm), it would be rational to evaluate the minimum and the maximum TOF time boundaries of the circuit. Using the kinetic energy equation (equation 2), one can find the TOF for a scattered neutron losing 50%, 90% and 99% of its energy to a proton in EJ-204. Table 2 shows the TOF calculations for a scattered neutron with original kinetic energies of 0.001 MeV, 0.01 MeV, 0.1 MeV and 1 MeV. The examples are used to illustrate the relation between the incident neutron energies, percentages of energy losses in the scattering reactions and the corresponding TOF. Based on this, one can estimate neutrons TOF that can be successfully detected in the TOF circuit and hence the minimum and maximum neutron energies that can be measured by the imaging. The table indicates that within the current TOF circuit, scattered neutrons with energies equal to or above 0.1 MeV will fall outside the TDC7200EVM measurement range if they lose 50% or less of their initial energies. Similarly, neutrons with incident energies lower than 0.001 MeV will not be detected by the TOF circuit if they lose 99% of their initial energy in the scattering reaction.

Table 2: Estimated neutron TOFs and velocities measured in the current prototype configuration.

	Neutron Energy (MeV)			
	1	0.1	0.01	0.001
Energy (MeV) and TOF after 50% energy loss after scattering (ns) (velocity m/s)	3.1 (9.8x106)	9.7 (3.1 x106)	31 (9.8 x105)	97 (3.1 x105)
TOF after 90% energy loss after scattering (ns) (velocity m/s)	6.9 (4.4x106)	22 (1.4x106)	69 (4.4x105)	220 (1.4x105)
TOF after 99% energy loss after scattering (ns) (velocity m/s)	22 (1.4x106)	69 (4.4x105)	220 (1.4x105)	690 (4.4 x104)

In addition, the TOF circuit generates a list of the digital addresses of all SiPM pixels that are activated, based on the first arrived/first recorded approach. This list will facilitate data reconstruction of the Compton camera and the neutron scattering sub-system since events generated in the SiPM array are time correlated according to their order of arrival. Figure 9 shows the direction of logical operations in the TOF board starting with arrival of pulses from the comparator board to the transmission of the activated 8-bit address to the USB2633 DAQ digital port.

The pulses from each comparator are simultaneously sent to a D-type flip-flop (MC14174M, ON Semiconductors) which will store a value of 1 when the corresponding comparator has a high output, at the same time as the clock (given by the output of the OR gate in level 3 – see Figure 9) is at a rising edge. The output of the flip-flop will return to 0 when the corresponding comparator has a low output at the next rising edge of the clock input. Note that the clear input pin on the flip-flop is always high, as this input is connected directly to a constant +12 V supply. The flip-flops are in groups of 8 and the outputs of the flip-flops in each group are sent to an 8-input 8-bit priority encoder (CD4532B, Texas Instrument) which encodes the location of whichever flip-flop has a high output to a 3-bit binary code output. This output represents the address of the corresponding SiPM pixel that has registered an event. Each encoder also has another output, GS, which goes high if any of the inputs are high, i.e. if an event was registered by any of the corresponding flip-flops. As 8 of these encoders are needed to encode the address of the 64 pixels, it is necessary to discriminate between the output of each encoder to acquire a unique complete address. The three binary outputs from each encoder (Q1, Q2 and Q3) are consolidated using three 8-input OR gates, resulting in a single 3-bit address. Furthermore, the GS outputs from each encoder are fed into another 8-input 8-bit priority encoder. The output of this encoder gives the address of the other encoders (0-7) that had registered an event. These two 3-bit addresses therefore uniquely identify the pixel that registered an event as it occurs. These six values are eventually saved in a .csv file, the data transferred via the digital input of the USB2633 DAQ. While each SiPM array has a corresponding TOF circuit, for the third layer it is only used to generate the digital address list. That is, there is not a TDC board connected to the third layer.
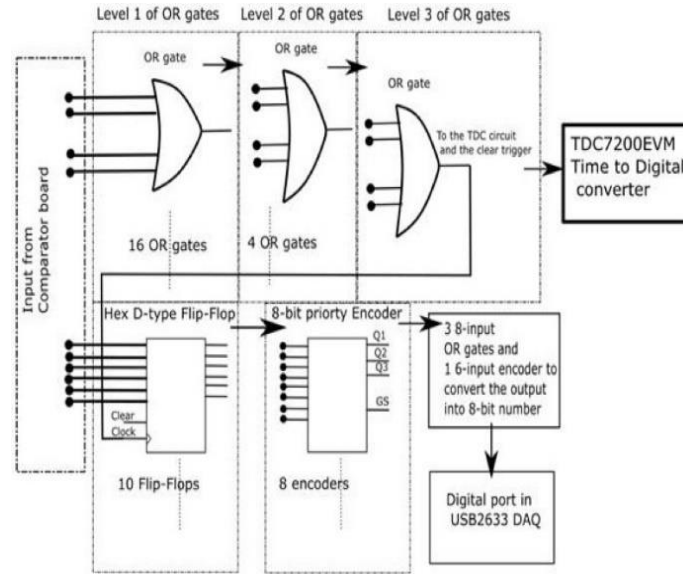

Figure 9: Architecture of the TOF board.

3.3   Control zone

In order to process the data coming from the ASRC, three pieces of software are used in this system. A Python code (v3.6.5) is first used to serially acquire the data from the 64 analog ports and 1 digital port from each of the three DAQs utilised. The code utilises the mcculw module [38] to communicate and read the data from the DAQs before saving the data from each layer in individual .csv files. The digital port in each DAQ reads the 8-bit digital data stream that contains the addresses of the pixels that have been activated and saves this in another.csv file. Also acquired here is the analogue TOF data stream generated from the TDC7200EVM module which utilises a LABVIEW GUI [39] to interact with the user and generate more .csv files in which TOFs are saved in general number format. In total, seven .csv output files are generated after the 60-second data acquisition cycle for the

activity of the sources described in the next section. Six of these output files use the Python code interface, while the TOF data is instead relayed to the computer via a LabVIEW™ interface. A MATLAB® [40] script has been developed for analysing and reconstructing the data from these seven .csv files. For each layer, the 8-bit addresses are converted into channel numbers and then using a while loop, the voltage is read from the analogue output files of the corresponding layer and assigned to the channel number. Depending on the type of event, the measured voltage are converted into energy, probability cones are created and the image plane reconstructed. The flowchart shown in Figure 10 illustrates the steps taken within the MATLAB® algorithm.
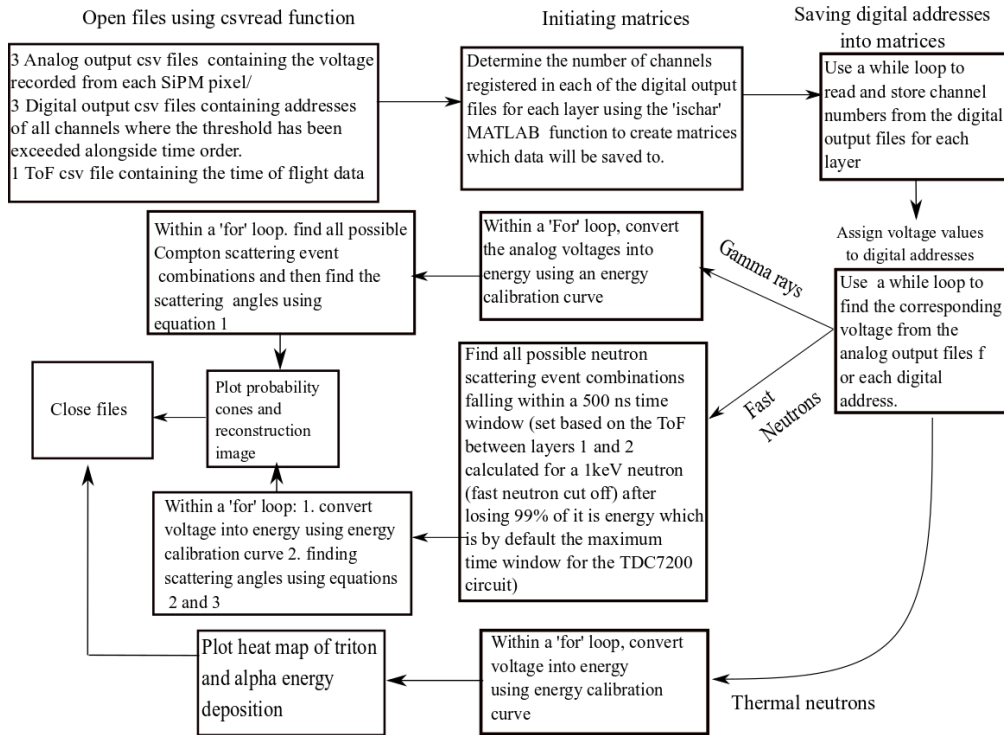

Figure 10: Flow diagram illustrating how the MATLAB algorithm creates the probability cones and construct source image.

3.4   Radioactive source details

Two sealed radioactive sources have been used for testing of the device; Cs-137 and Cf-252. The Cs-137 used had a total activity of 315 kBq at time of use. A high proportion (94.7%) of the beta particles produced during its decay lead to Cs-137 disintegrating to an excited state of barium, which decays subsequently via a 662 keV gamma-ray, corresponding on this basis to a total of 300,000 gamma rays emitted by this source each second. The Cf-252 source at Lancaster University is encapsulated with aluminium and had an activity of 18.8 MBq at time of use. This source is held inside a double-walled, fiberglass tank of water of volume ~1 m^3 that, in turn, is located inside a mild-steel enclosure. Cf-252 decays via either α emission or spontaneous fission, with a branching ratio of 96.91% and 3.09%, respectively [41]. 3.759 neutrons on average are emitted per spontaneous fission event, thus yielding a total number of 2.18 x 10^6 n/s into 4π with an average energy of *c.a.* 2.1 MeV, and most probable energy of *c.a.* 0.7 MeV [42]. The average energy of the associated gamma-ray component is 0.8 MeV with average prompt fission multiplicity of 8.3 gamma rays per fission event [43].

4   Experimental Setup

Figure 11 shows the experimental setup with detector enclosure assembly (front-end), voltage supplies and the readout electronics ASRC. Using a Gaussian fit of the normalised pulse height against voltage; the 662 keV gamma-ray photo-peak was detected in the lithium glass at 0.36 V and resolution in terms of a FWHM of (0.23 ± 0.02) V. Similarly within CsI(Tl), the 662 keV gamma-ray photo-peak was detected at 0.44 V and resolution in terms of a FWHM of (0.37 ± 0.01) V. Figure 12 shows a plan schematic of the experimental setup used for the

neutron measurements. The source-to-detector enclosure distance can be broken down into several components. First, there is the 50 mm distance between the detector enclosure and the source tank, and then there is a 242 mm gap between the Cf-252 source and the edge of the tank. This equates to a total source-to-detector distance of 292 mm. However, for simplicity, the source tank to detector enclosure distance (50 ± 1) mm is defined for the rest of this paper as the source-to-detector distance.
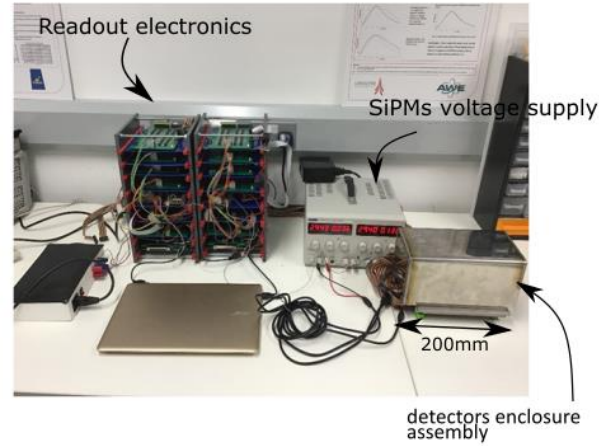

Figure 11: A photograph of the gamma-ray detection experiment setup. The sealed Cs-137 gamma source will be positioned just out of view of this photograph, on the right-hand side.
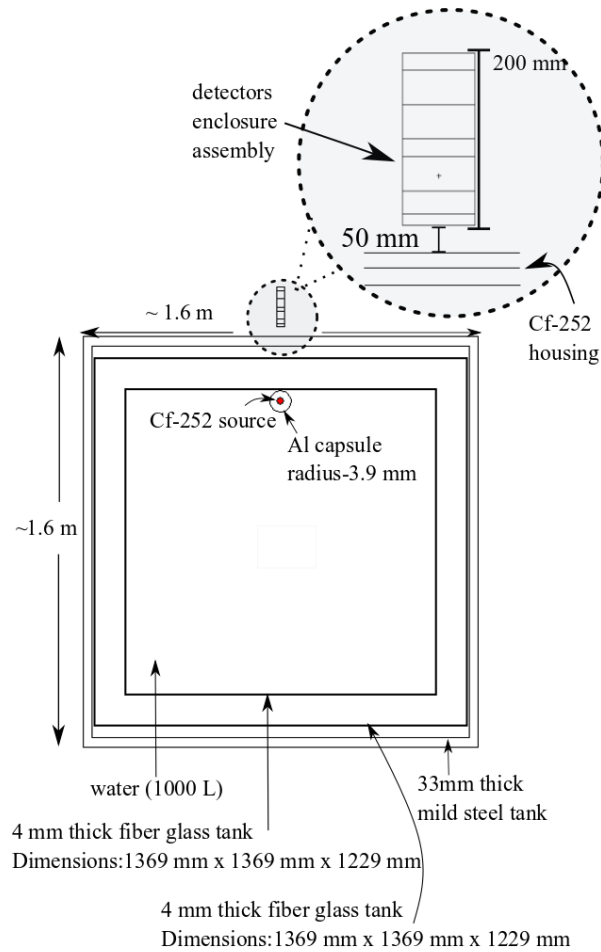

Figure 12: A plan view (schematic) of the experimental setup for the neutron measurements performed in this research.

5   Monte Carlo Simulations

The system was designed and verified using Monte Carlo simulations in MCNPv6.1.0 [44]. The cross sections used in this work for neutrons simulations are from the ENDF/B-VII.1 library, with room temperature assumed throughout (293K). For gamma-ray analysis, the Evaluated Photon Data Library (EPDL) and the Activation Library (ACTL) compilations from Livermore data libraries were used [44]. In all subsequent simulations, the geometry of the detection system and material characteristics were as defined in section 2. In addition, the absence of significant levels of background radiation within the experimental setup allows the comparison of experimental measurements with simulation results and enables the verification of experimental results. The analysis for all radiation types described here is based on the output of the PTRAC card, FMESH tally and F8 pulse height tally. Adding the PTRAC card to an MCNP input file creates an output file detailing particle tracks through the system with complete information of collisions and interactions depending on the keywords added to the input card. An overview of the cards used in the PTRAC file, FMESH card and F8 tally are shown in Figure 13, illustrating the layout of the output files with brief highlights of the main elements. The PTRAC input file includes the output control keyword FILE=ASC that instructs the software to generate an ASCII output file type, with the command WRITE=ALL indicating that the location in Cartesian coordinates and directional cosines of the particle should be written to the output file along with the particle energy for each interaction, the weight and the time. The control keyword TYPE=n, p, t, a, h specifies the particle types in the PTRAC output file (denoting neutrons, photons, tritons, alpha particles and protons, respectively). Furthermore, the control keyword MAX=100000 controls the maximum number of events to be written within the PTRAC file. The output file generated by the use of the PTRAC card is subsequently analysed in MATLAB®.

The FMESH card generates a user-defined mesh tally laying over the surface or cell of interest with Cartesian geometry used throughout the FMESH based simulations. For the Monte Carlo simulations used in this research, the main facets of the scintillators in the detector module are defined in the y-z plane, and hence the locations of the fine mesh points are specified in these two directions, with keywords JINTS=60 and KINTS=60 defining 60 fine mesh points in each orientation. The F8 tally is defined in MCNP6 as a pulse-height tally, and thus the output of this tally is a register of the energy distribution of pulses within a cell by the defined radiation particle and any subsequent secondary particles. In contrast to the case of photons, when neutrons are evaluated using the F8 tally, an inconsistency can arise because of differences in the way neutrons transport through matter. To overcome this error, the F6 MCNP energy deposition tally (in units of MeV/g) is used to determine the secondary particles generated by a neutron interaction. For example, the triton and alpha generated as a result of neutron capture in Li-6, is used in coincidence with the F8 tally with a pulse-height light tally with the anticoincidence (PHL) option added to the tally specification card (FT). The following MCNP code is an example of an F8 tally card executed to generate a distribution of pulses from neutrons capture reactions in lithium glass through the interactions of the secondary particles:

- F6:a (cell number)
- F16:t (cell number)
- F8:a (cell number)
- FT8 PHL 1 6 1 LIG-1
- F18:t (cell number)
- FT18 PHL 1 16 1 LIG-1

LIG-1 and CSI-1 are keywords for the lithium glass and CsI(Tl) detectors that enable the use of a special tally treatment used when scintillators are selected. The numbers following the tally number, FT and PHL are the F6 tally number for this detector region followed by the pairing numbers of the tally number (6 or 16) and the tally bin number, which is the one in the example given here. More details of these keywords is available in the MCNP manual [45]. The way the cones are plotted can be described in several stages:

1) The PTRAC file is imported into the MATLAB environment.

2) The number of histories is ascertained in order to initiate counting matrices.

3) Using a 'while' loop and 'If' statement, events of interest are determined.

4) The appropriate equations are used to find scattering angles and energies of gamma rays and neutrons (see section 2).

5) Cones are plotted leading to probability map generation.
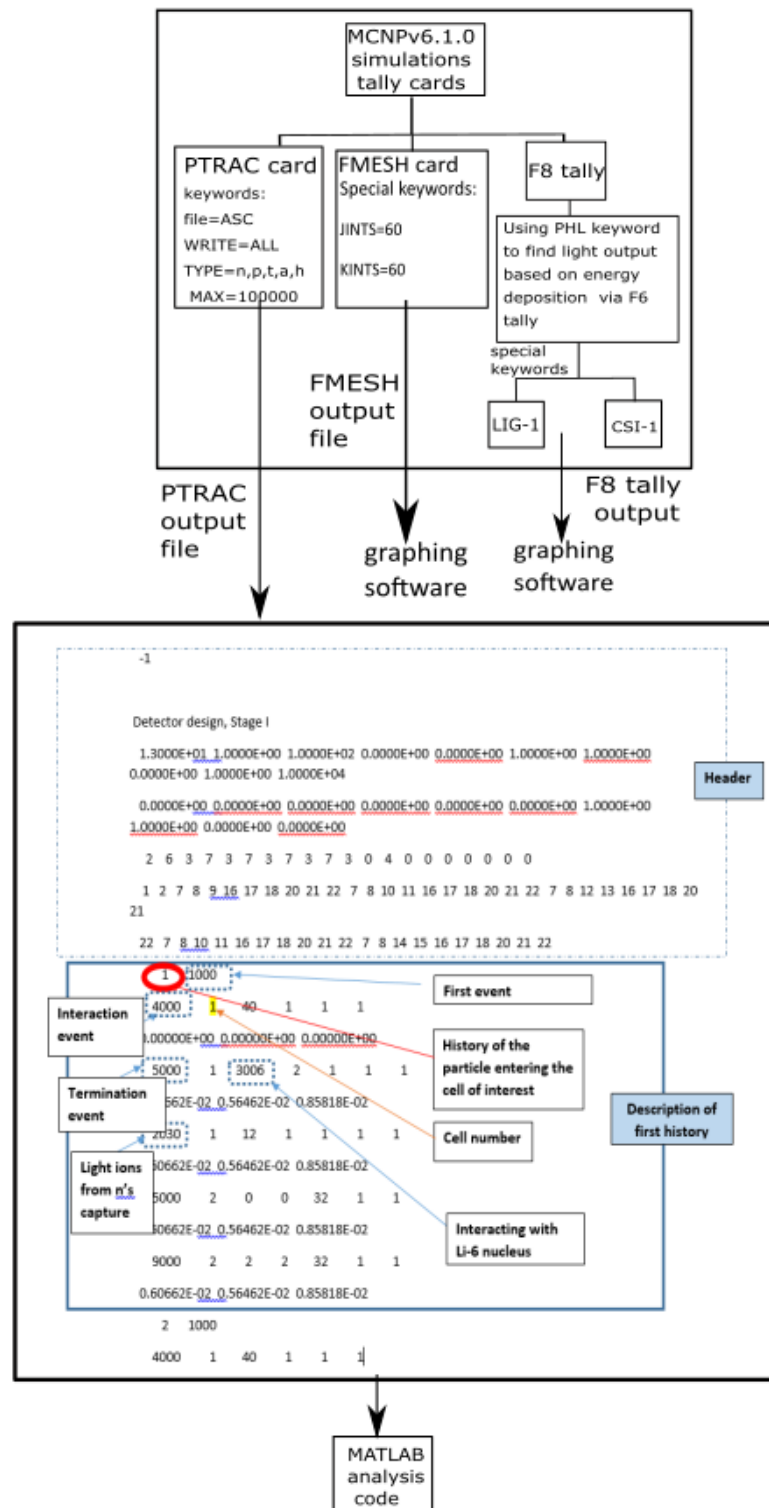

Figure 13: A schematic diagram illustrating MCNPv6.1.0 input parameters and simulation output analysis.

5.1 Simulation results for the gamma-ray detection system

5.1.1 Detection efficiency of the Compton-scattering sub-system and the localisation of a gamma-ray source

Simulations of the complete front-end system exposed to a single Cs-137 source (as defined in section 3.4) were conducted. The number of particles specified in the MCNPv6.1.0 environment was 298,305, with 1106 of these events registered in the PTRAC output file. The positions, the energy deposited by gamma-ray interactions and the associated scattering angles were determined within the layer 2 15-mm lithium glass and layer 3 CsI(Tl), using a combination of the MATLAB code described above and equation 3. The output is illustrated in Figure 14 with the source located centrally 50 mm in front of the first detection layer; denoted here with an 'X'. It can be observed visually here that the pixel located at (3, 5) shows the highest probability of source location, a position within one pixel of the actual location; a distance of 3.375 mm. Due to the statistical nature of this technique, it is necessary to consider the surrounding pixels of the actual source position. The intensity in the pixel of the actual source location and the 16 pixels surrounding it combined is (31.2 ± 0.5) % of the total predicted fluence – an average of 1.95% in each pixel. The pixels outside this area receive on average 1.43% of the total predicted fluence each. Thus, there is a rise of 36% in the pixels around the correct source location. The intrinsic efficiency has been simulated too indicating the total number of radiation quanta detected in the Compton scattering sub-system of 13 events per second (a figure verified using repeated simulations). Given the detector cross sectional area (7.29 cm$^{2)}$, an estimate of the geometric efficiency of the detector of 0.023 follows. Given the activity of the Cs-137 source, 6,861 photons would be expected to reach the active detector surface in the specified period of time. Thirteen events recorded indicates an intrinsic efficiency of 1.89×10^{-3} at 662 keV.
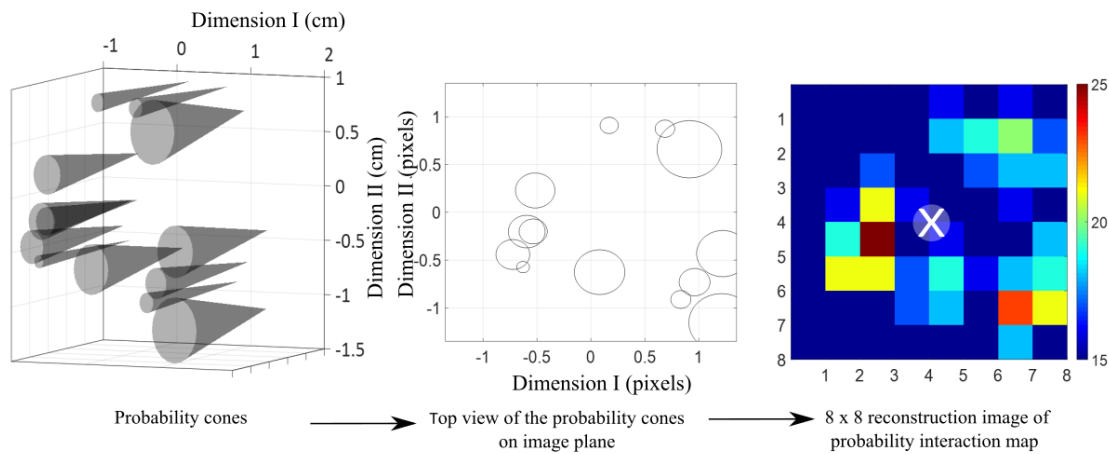

Figure 14: A schematic diagram illustrating the steps of image reconstruction applied to yield the response of the system to a gamma-ray source ('X' indicates the source location in simulations). The intensity units are arbitrary.

5.1.2 Source localisation ability of the Compton scattering sub-system

The source localisation ability of the Compton scattering sub-system was determined using the Cs-137 source placed at four different locations, relative to the front of the detector system, as illustrated in Figure 15, with the results shown in Figure 16. The pixel corresponding to the real location of the source, along with the 8 surrounding pixels, represents 63.9% of the total fluence recorded by the camera, an average of 7.1 ± 0.1 % per pixel compared to 0.7% of the total fluence on average per pixel outside of this area. Similarly, Figure 16 (b) indicates 69.3% of the fluence in the nine pixels around the real source location (7.7 ± 0.2 % per pixel compared to 0.9% outside of it), Figure 16 (c) shows 60.3% of the fluence in the nine pixels (6.7 ± 0.1 % compared to 0.7% outside of this) and finally Figure 16 (d) shows 71.1% of the fluence observed from within the nine pixels surrounding the real source location (7.9 ± 0.1 % compared to 0.9% outside of this area).
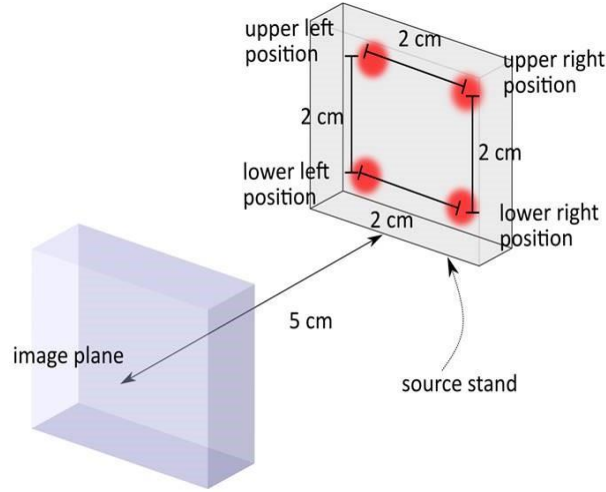
Figure 15: A schematic diagram of the four different locations of the Cs-137 source relevant to the image plane.
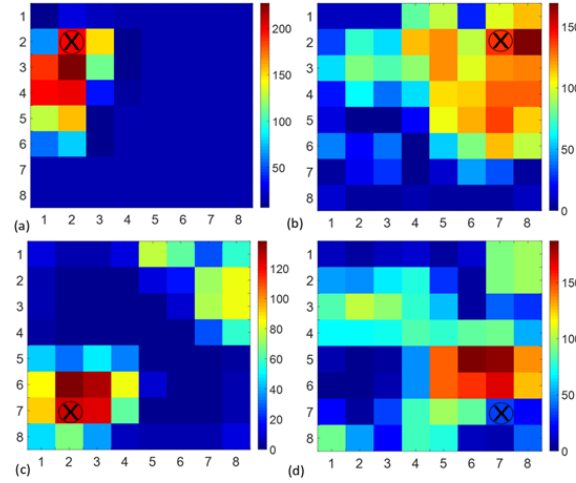

Figure 16: The reconstructed images derived from the results of simulations of the response of the system to changing the position of the Cs-137 source (a) upper left, (b) upper right, (c) lower left and (d) lower right. The colour map indicates image intensity and ⊗ the source position in the simulations relative to the imaging system.

5.1.3   Angular resolution of the Compton scattering sub-system

The ability of the system to differentiate between two, closely-spaced gamma-ray sources was investigated in order to estimate the angular resolution of the system. Three different angular spacing scenarios were explored, namely 40º, 15º and 5º. The resulting reconstructed images with two Cs-137 sources 40º (29 mm) apart, 15º (10.5 mm) apart and 5º (5 mm) apart are shown in Figure 17. The number of PTRAC events recorded was 1736. In Figure 17 (a), the points at which the ellipses intersect appears to be shifted upward relative to the location of the source defined in the simulation geometry. Nonetheless, these results indicates that the system can differentiate between two sources with a minimum angular spacing of 15º.
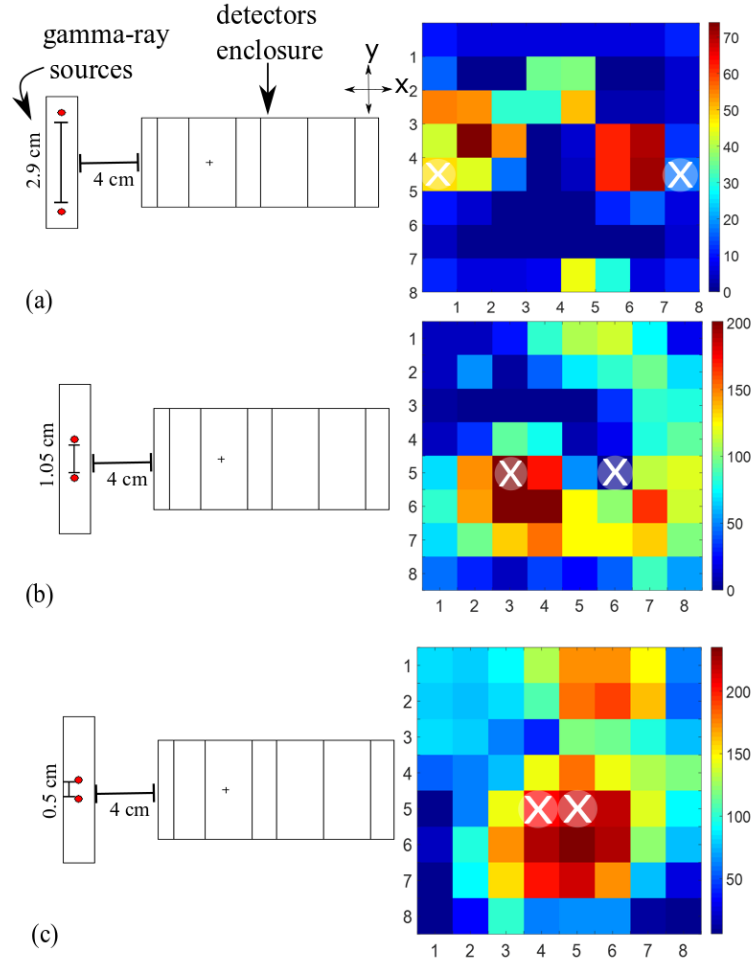
Figure 17: A schematic diagram of source position with respect to detectors enclosure and the reconstructed images of the computational analysis of two Cs-137 sources 40° (29 mm) apart, 15° (10.5 mm) apart and 5° (5 mm) apart (colour map shows image intensity and ⊗ indicates source location specified in the simulation geometry).

5.2   Simulated results using the thermal neutron detection system

The response of the system exposed to thermal neutrons was simulated using the Cf-252 source set-up as illustrated in Figure 12. The Cf-252 source is defined using the Watt approximation of the corresponding fission spectrum using the Spontaneous Fission (SP) keyword with appropriate constants in the source card [33]. In order to generate a high proportion of thermal neutrons, an 11-mm thick polyethylene slab was included in the simulation geometry between the instrument and the source tank to act as a moderator. The F2 card was utilised in the MCNPv6.1.0 input file to estimate the number of thermal neutrons incident on the instrument. Considering the number of neutrons output from the polyethylene slab is 4.16×10^{-6} per initial neutron, the thermal neutron fluence was determined to be 81 n/cm^2 over the 60 s period. Therefore, the expected number of thermal neutrons is 591 over the whole of the 2.7×2.7 cm detector area. The F8 tally card was added to the MCNPv6.1.0 input file which was used to investigate the number of triton particles generated by the thermal neutrons capture reactions and subsequent energy pulse height generation in the lithium glass detector. The details of the F8 tally card used in the input file are indicated in section 5. In the Monte Carlo environment, 478 tritons are simulated as being generated within the lithium glass layer indicating a simulated intrinsic efficiency of $(81 \pm 4)\%$.

5.3   Simulation results for fast neutron detection system

The response of the system when located 50 mm from the front of the Cf-252 neutron source tank was simulated using the PTRAC card to generate the data required in equations 2 and 3, using the keywords listed in Figure 13. The parameters registered in the PTRAC output file included interaction positions, energy depositions and TOF data. Equations 2 and 3 were then used to find the scattering angles and to generate the probability cones, as shown in Figure 18. Based on these simulations, 8177 neutrons reached the detectors enclosure, 50 of which were recorded in the system as neutrons scattering events. This indicates an intrinsic detection efficiency of 6.1 x10^{-3} at 2.1 MeV (the average energy of neutrons from Cf-252 source).
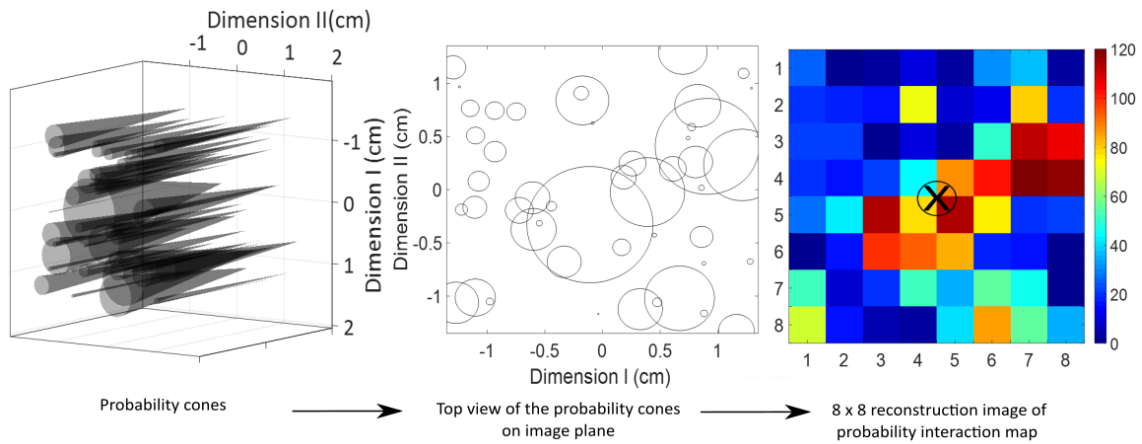

Figure 18: A schematic diagram illustrating the steps taken in image reconstruction to extract the response of the system to the neutron source (⊗ is source location defined in the simulation geometry).

Figure 18 would suggest that the source is a scattered source with only 27.2% of the neutron flux predicted to be within one pixel of the real source location in this result. This can be compared to Figure 14, which illustrated a Monte Carlo simulation of the probability map achieved when the Cs-137 source was located 50 mm in front of the instrument. As expected, the Cs-137 results illustrate a point source as oppose to a scattered source.

6   Experimental results and discussion

6.1   Gamma-ray results

The experimental gamma-ray results are divided into three sets: the first two sets focus on the validation of the system exploiting Compton scattering to detect and locate gamma rays, and the third set on the abilities of the system to locate and differentiate different gamma-ray sources. Keeping in mind the activity of the gamma-ray source describe in section 3.4, all measurements (unless specified) were made over a 60 s time interval and repeated three times to yield an average. The uncertainties depicted by the error bars were determined in each case on the basis of one standard deviation of the mean in these results. The usual compromise, i.e. longer scan times yield more statistics and thus reduce uncertainties, has been sought. However, shorter scan times may be desirable in some applications where a faster camera may be preferable to one offering greater accuracy.

6.1.1   Compton events as function of time

The probability of Compton scattering events as a function of time was determined experimentally to determine the efficiency of the system. Figure 19 indicates the total number of Compton scattering events, which occur in the system as a function of time when the Cs-137 source is 50 mm away from the front detector plane. An average of 2.03 ± 0.01 events was observed per second whereas; the geometrical efficiency of 0.023 implies 6900 gamma-ray photons were incident on the detector surface. The figure of 1.98 thus indicates an intrinsic efficiency of (2.89 ± 0.07) x 10^{-4} at 0.662 MeV. This figure is consistent with the experimental reported value in the work done by

Poitrasson-Rivier et al. [22] who also reported an efficiency in the order of 10^{-4}. This measured efficiency is 15 % lower than the MCNPv6.1.0 results in section 5.1.1.
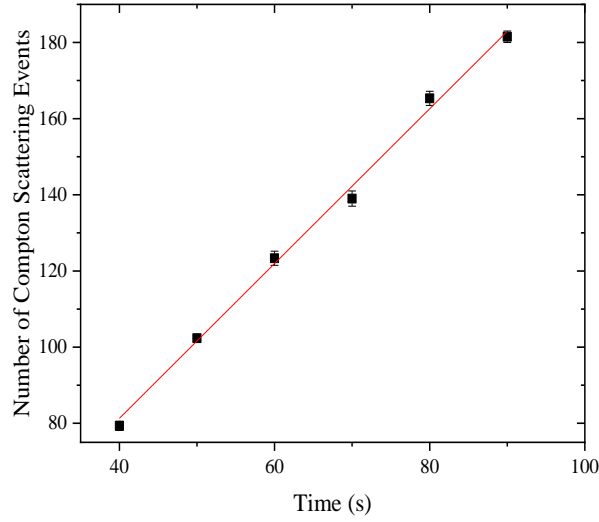

Figure 19: Number of Compton-scattered events versus time for the Compton scattering sub-system. The fit of the points indicates a linear relationship between the number of Compton scattering event and time with slope of (2.03 ± 0.01) counts per second and R^2 value of 1.0

6.1.2   Compton events as a function of distance

For further confirmation of the successful operation of the system, a graph of the count rate as a function of distance is provided in Figure 20. The inverse-square law would suggest that the exponent in the fit line would be -2 instead of -2.28 ± 0.01.
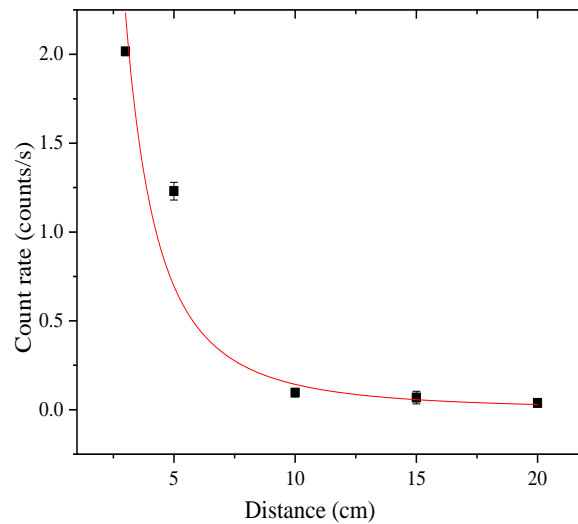

Figure 20: Count rate vs. distance for Compton camera subsystem. The fit an exponential decay with decay constant of (-2.28 ± 0.001) counts/cm and R^2 value of 0.99.

6.1.3   Source localisation ability of the Compton scattering sub-system

In order to verify the ability of the system to identify individual sources and to locate the source position, the Cs-137 source was moved to four different locations close to the four different corners of the active area of the system, and 50 mm from the image plane, as illustrated in Figure 15. The system responds to this change in source position with relatively high accuracy as illustrated in Figure 21, in which reconstructed images as a function of changing

source position are presented. It can be seen that the location of the source is identified successfully in each scenario. Figure 21(a) shows that 26.0% of the predicted flux is within one pixel of the real source location. The corresponding value is 35.4% in Figure 21(b), 43.3%, in Figure 21(c), and 34.2% in Figure 21(d). This appears to indicate relative consistency across all four locations with between 26.0% and 43.3% of the flux correctly predicting the source location to within a pixel. Another way to quantify these results is to compare the peak-to-average values. In (a) the maximum value is 25, compared to a total fluence over the 64 pixels of 600, an average of 9.2. This indicates a peak-to-average figure of 2.7, with corresponding figures of 7.8, 5.7 and 2.8 for results (b), (c) and (d) respectively. The equivalent simulated results shown in Figure 16 indicated that between 46% and 64% of the total predicted fluence was within one pixel of the real source.
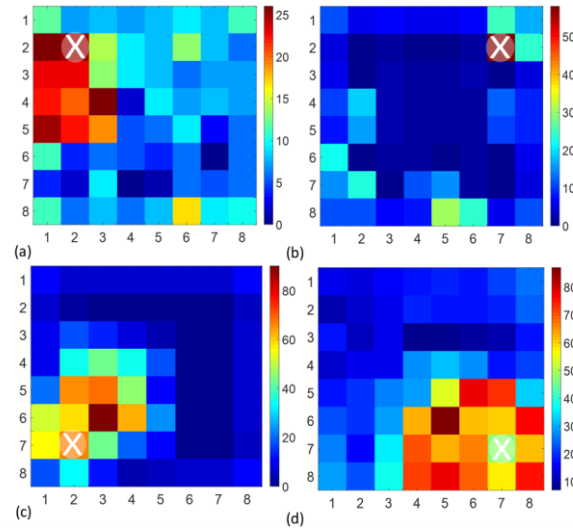

Figure 21: Reconstructed images of experimental results of the system response to four, different Cs-137 source positions: (a) upper left, (b) upper right, (c) lower left and (d) lower right. ⊗ marks the source position in the experiment relative to the imaging system.

Experimental results reported here are comparable with MCNPv6.1.0 simulations results (section 5.1.2) in terms of locating the source within the right image plane corner. However, lower predicted fluence in the pixels surrounding the actual source locations in the experimental results might be due to limitations in the efficiency of the imaging system compared to the simulation environment were all events are recorded in the PTRAC file.

6.1.4   Angular resolution of the Compton scattering sub-system

Two identical Cs-137 sources were used to determine the ability of the system to differentiate between two closely-spaced, gamma-ray point sources. Figure 22 indicates the geometry of the three experiments via plan diagrams, alongside the corresponding reconstructed images with two Cs-137 sources 40° (29 mm) apart, 15° (10.5 mm) apart and 5° (5 mm) apart. It is clear that in situations (a) and (b) the sources can be discerned from one another, whereas in situation (c) the two are indistinguishable, indicating that the angular resolution of the system is probably between 15° and 5°. Another way to look at these results is to look at the maximum value recorded compared to the lowest value between the two peaks. In these three scenarios, the lowest to highest values recorded were 4.0%, 7.4% and 100% in the 40°, 15° and 5° scenarios, respectively. Although the simulated (shown in section 5.1.3) and practical results are not identical, the outcomes are similar in that the system's angular resolution is in the order of 15°. The discrepancy in the results might be due to limitations in the efficiency of the imaging system.
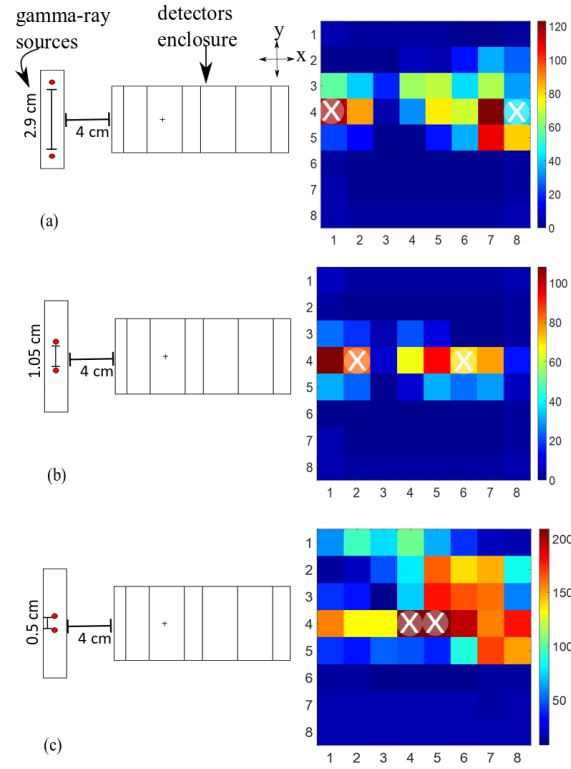
Figure 22: A schematic diagram of source position with respect to the detector enclosure and the reconstructed image of two gamma-ray sources 40º (29 mm) apart, 15º (10.5 mm) apart and 5º (5 mm) apart (colour map shows image intensity and ⊗ indicates source locations).

6.1.5   Gamma source within transportation devices

One of the main goals of this research is to test the capability of the design to detect and locate radiation sources in real-time in security applications. To fulfil this goal, trafficking scenarios of hidden gamma sources have been replicated using two realistic transportation devices. Initially, an IM2720 Peli® case [46] made of ABS plastic with an average thickness of 12 mm and external dimensions of 432 mm × 553 mm × 254 mm was used as an example transportation device. These cases are toughened specifically to enable transportation of expensive and delicate items such as instrumentation equipment. Secondly, a shipping box made of cardboard with a thickness of 9 mm and external dimensions of 255 mm x 260 mm x 260 mm was used. Figure 23 provides some photographs of the experimental setup and the response of the system to these two scenarios using Cs-137 sources. The results indicate that the instrument can detect and locate a CS-137 source successfully, either within a Peli® case or a cardboard box within 60 s for gamma sources of ~300 kBq. In both cases, the probability map indicates that the source is predicted to be either at its real location or within the adjacent eight pixels.
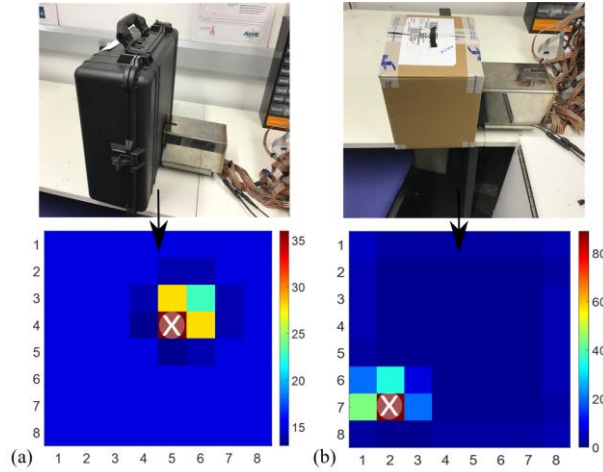
Figure 23: The experimental setup (top) and system response (below) to a hidden Cs-137 source in (a) Peli® transportation case and (b) cardboard shipping box with colour bars showing image intensity in arbitrary unit (⊗ is the source location in the experiment setup).

6.1.6   The gamma-ray component of the Cf-252 source

Here, the gamma-ray Compton camera sub-system was isolated and utilised to monitor the gamma-ray component of the Cf-252 source. A 60-mm thick slab of polyethylene was placed between the instrument and the source in order to block a significant proportion of the neutron output from the source, allowing a significant gamma ray component to reach the detector with reduced neutron fluence. Figure 24 shows the experimental setup in the laboratory and illustrates the combination of the Cf-252 source, polyethylene slab and instrument. Figure 25 shows the Compton scattering sub-system response map obtained with this experimental set-up. It should be noted that, within this output, results in the upper-right corner of the instrument are shadowed by the stainless steel enclosure.
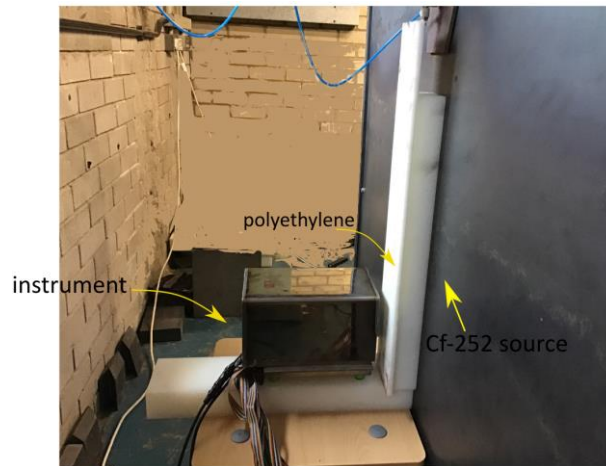

Figure 24: A photograph of the experimental setup for the gamma-ray experiment with the detection instrument, polyethylene slab and Cf-252 source tank.
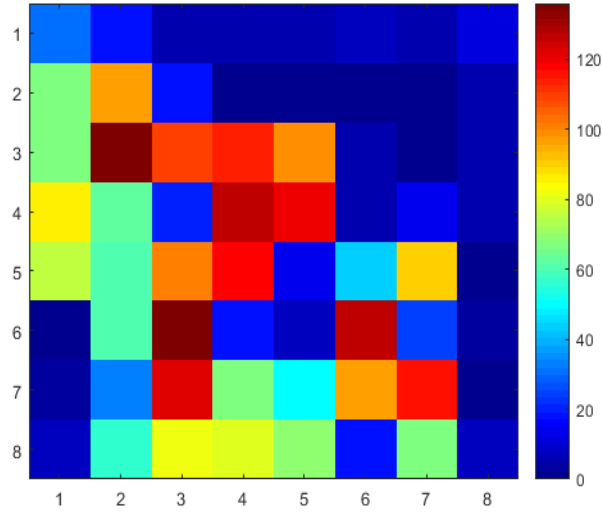
Figure 25: The reconstructed Compton-scattering, sub-system response to the gamma-ray component from Cf-252 with colour bars showing image intensity in arbitrary unit.

6.2   Thermal neutron testing

To investigate the system response to thermal neutrons, an 11-mm thick polyethylene moderator was placed between the instrument and the Cf-252 source tank in order to thermalize the neutron fluence. The response of the system is shown in Figure 26. As described in section 5.2 above, the expected number of thermal neutrons incident on the detector as estimated via MCNPv6.1.0 simulations is 600 neutrons/s. Taking an average from five repeated experiments, the number of pulses generated in the lithium glass detector in the first layer is (460 ± 20) neutrons/s. Based on these calculations, the measured intrinsic detection efficiency is (78 ± 4) %, compared to the simulated value of (81 ± 4)% from section 5.2. Work by G. Ban et al [47] reports a comparable detection efficiency of 80.6 ± 2.3% in GS10 for low energy neutrons in the ultra-cold region.
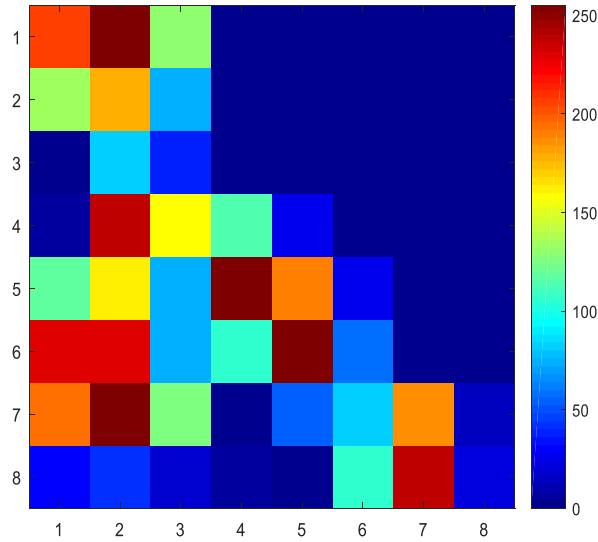

Figure 26: Reconstructed systems' response to thermal neutrons from Cf -252 source with colour bars showing image intensity in arbitrary unit.

6.3 Fast neutron testing

6.3.1 The response to fast neutrons

The response of the neutron scattering sub-system was investigated by measuring the number of fast-neutron scattering events as a function of time at 50 mm from the Cf-252 source. Figure 27 indicates the number of fast-neutron scattering events in the first two layers as a function of time with the number of events increasing linearly as expected. 2.18×10^6 neutrons produced per second by the source multiplied by the calculated geometrical efficiency of 0.00258 indicates an expected 5,600 neutrons/s incident on the active area of the detector. Figure 27 indicates that an average of (4.2 ± 0.1) events are being recorded per second, a figure that equates to an intrinsic efficiency of $(7.49 \pm 0.2) \times 10^{-4}$. This number roughly compares with the detection efficiency reported by Poitrasson-Rivier et al. [22], which was of the order 10^{-4}.
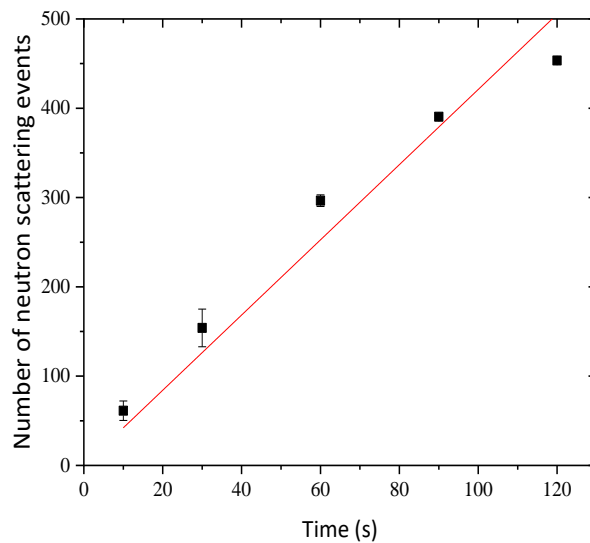

Figure 27: Neutron scattering events as function of time in the neutron scattering sub-system. The fit of the points indicates a linear relationship between the number of neutron scattering event and time with slope of (4.2 ± 0.1) counts per second and R^2 value of 0.99.

6.3.2 Collimated and un-collimated neutron beams

The response of the system was further investigated using alternate source geometry. Figure 28 shows a comparison of the system response between the standard non-collimated Cf-252 source and a collimated pencil beam, with 50 mm between source and detection plane. The collimated version was formed using 50 mm thick polyethylene slabs with an 8 mm diameter hole. Results achieved indicate quite clearly through simple visual inspection the change in the system's response to the source geometries. As expected, the counts when collimation is not used are generally far higher than in the collimated version. The result for the un-collimated source, indicate that 26.3% of the predicted radiological source is correctly assigned within one pixel of the real source location. This compares to the collimated source where 55.0% of the predicted radiological source is assigned correctly to within one pixel of the real source. An alternative way to report this is to say that in Figure 28(a) the peak to average figure is 3.99 where as in Figure 28(b) the figure is 8.56. This indicates the ability of the neutron detecting subsystem to detect both a point source (emitting neutrons over 4π) and a beam-like source geometry.
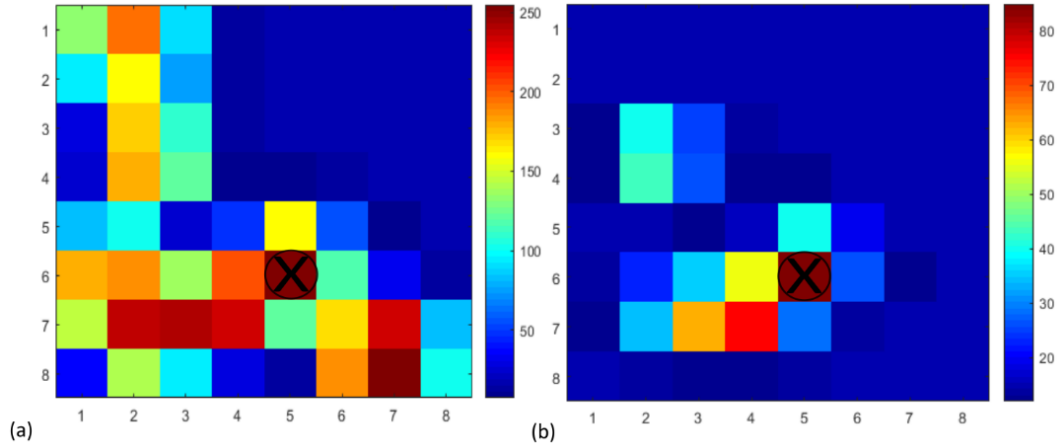
Figure 28: Reconstruction images of neutron scattering sub-system response to (a) non-collimated and (b) collimated Cf-252 source (colour bars shows image intensity).

7   Discussions and Future Work

For gamma-ray photons at energy of 662 keV, MCNP6 simulations indicated intrinsic detection efficiency in the order of 10^{-3}, whereas experimental results showed detection efficiency in the order of 10^{-4}. Similarly, for neutrons emitted from Cf-252 source, MCNP6 simulations indicated intrinsic detection efficiency in the order of 10^{-3}, whereas experimental results indicated intrinsic detection efficiency of 10^{-4}. In both cases, the differences between simulation results and experimental results are anticipated to be due to the limited speed of the DAQ. For thermal neutrons, simulation results indicated intrinsic detection efficiency of (81 ± 4) % compared to the experimental results demonstrating intrinsic detection efficiency of (78 ± 4) %. In here, the experimental result falls within the range of the MCNP6 simulation result. The prototype instrument fulfils the criteria of detecting both gamma rays and neutrons within a relatively short time period of 60 seconds for gamma sources of ~300 kBq and neutron sources of 10^6 neutrons per second in close proximity of <300 mm. However, there are some significant issues and limitations: The testing that has been undertaken has involved source locations close to the detection plane. If the sources were located at a more realistic distance from the instrument, it would be expected that the statistics would be reduced significantly. The efficiency that has been recorded in both the gamma-ray and neutron cases is of the order 10^{-4}, which is comparable to efficiencies reported in other multi-layered Compton scattering imaging systems. Spatial resolution of the instrument has been estimated at <15% and more >5%, although the exact figure is difficult to ascertain due to the digitisation of the visual results achieved. So where does this instrument sit in comparison to other neutron and gamma localising instrumentation? The Germanium Gamma Ray Imager [9] has been developed at the Lawrence Livermore National laboratory, with dimensions of 300 mm x 150 mm x 230 mm and a mass of 15 kg. The sensitive range is reported as between 30 keV and several MeV, with Compton scattering techniques also used within the instrument at higher energies (>150 keV). Spectral resolution s reported at being 2.1 keV (at 662 keV) with spatial resolution reported as being at 6 % [9]. The Gampix [6-8] is another gamma camera (known commercially as ipix) created at CERN and based on a coded mask and cadmium telluride sensor attached to a medipix 2 segmented photon counter. The instrument only weighs 1 kg and, dependant on rank of coded aperture chosen, offers spatial resolution of between 1.5 and 2 %, and an energy range of between around 59 keV (i.e. the Am-241 peak) and 1.25 MeV (i.e. the Co-60 peak). The Advanced Portable Neutron Imaging System (APNIS) was developed at Oak Ridge National Laboratory in order to initially detect and locate 14.1 MeV neutrons generated by a D-T source. The neutron detection part of the system consists of an 8×4 array of fast plastic scintillators segmented into 100 pixels that are read by four photomultipliers whose shared response determines the pixel of interaction [48]. The Radscan 2 system developed by Whitney et al. [5], involves the use of a coded aperture and a CLYC scintillator. Although numerical results are limited, visually the work presents very impressive images when either gammas or neutrons are solely utilised. Goldsmith et al. [49] report a 40 kg instrument which utilises Compton scattering to localise gamma rays and the time of flight between two layers of EJ-309 liquid scintillators to localise neutrons, and present an efficiency of 45%. The work of Gamage et al. [50] also presents some visually impressive images although values for parameters such as spatial or spectral resolution are not readily available in the literature. The paucity of comparable numerical data within the literature thus renders it difficult to perform a thorough comparison of individual instruments.

There are several improvements, which may benefit the instrument in its current state. A larger detection plane than the current 27 mm x 27 mm may be an obvious implementation to improve efficiency. The current photon sensor in a 2 x 2 configuration would suggest a geometrical efficiency improvement of a factor 4 times, although there will always be a trade-off between portability and detection efficiency. Utilisation of longer scan times would obviously improve statistics whilst diminishing significantly one of the strengths of the device. Use of an Application Specific Integrated Circuit (ASIC) could allow integration of all of the circuits within one PCB that could in turn be integrated within the system enclosure, thus minimising the overall footprint of the system and enhancing the mobility. However, such a solution can be financially restrictive in an instrument designed to be cost effective.

The TOF circuit currently presents a problem when false-positive scattering events occur. Currently, the process involves a start signal generated in layer 1 and an independent stop signal generated in layer 2. Therefore, if a neutron passes through layer 1 without interaction and then interacts in layer 2, an orphan stop signal is generated and thus false-positive events are recorded. With the probability of successful neutron scattering events estimated to be of the order of 10^{-4}, this can have significant impact on the performance of the system. A proposed solution to this shortcoming is in the addition of a trigger circuit such that a stop pulse is only generated if a pulse is first recorded in layer 1, and if a pulse exceeds the threshold voltage set by the comparator board. Another potentially significant area of improvement is in the increase in the measurement range of the TOF. The TDC7200EVM module has a measurement range of between 12 ns and 500 ns where, based on Table 2, scattered fast neutrons with scattering energies of around 0.1 MeV and above may fall outside of this range. A wider TOF measurement range can greatly improve the energy range of detected fast neutrons by the system.

Further, instead of interrogating each individual pixel, pulses could be integrated over each row and column of the SiPM array. This alteration to the current configuration could reduce power consumption in the overall circuit while maintaining the pixelated integrity of the system. In addition, because more current is allowed in each integrated row or column, the response of the circuit to deposited energy will show enhanced linearity. The signal from each row/column can be then sent to a reduced number of 16 filter and amplifier circuits for each layer of the design, reducing current consumption by a factor of four. Currently, four PCBs are utilised per layer with 64 channels filtered and amplified simultaneously, which can result in large and unbalanced currents drawn from the voltage supply. This sometimes causes an unbalanced current problem which can have a significant impact in the amplitude of the resultant signals and hence the energy resolution of the detected pulses.

The means of discriminating neutron and gamma pulses represents the most significant future work in this dual particle imaging system. The Pulse Shape Discrimination (PSD) principle [51, 52] is based on the differences in shape between the pulses from the scintillation process that are produced due to the interaction between the target radiation field and detection medium; an area of research well investigated in literature [53-58]. The shape and the height of the pulses depend on the interaction mechanism between the radiation and the detection medium, the energy of the incident radiation field and the light production mechanism in the medium [53]. Figure 29 shows time dependent differences for gamma-ray and neutron pulses in lithium glass as an example.
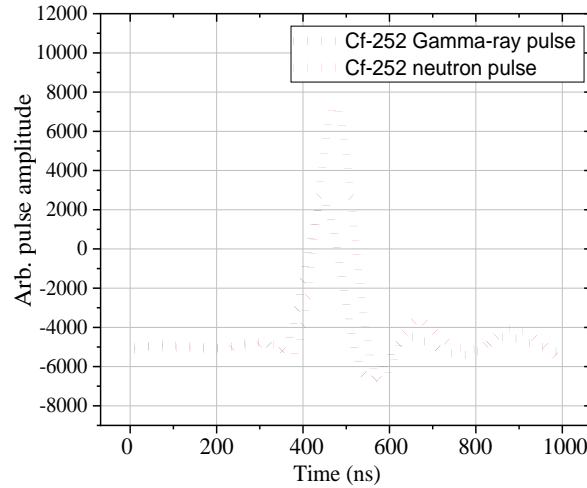
Figure 29: Raw gamma-ray and neutron pulses from Lithium glass crystal (GS10).

EJ-204 was utilised within this system to scatter fast neutrons, as it is a general-use plastic scintillator, although it is somewhat sensitive to low-energy gamma rays, and thus more sophisticated pulse-shape analysis may be necessary if this scintillator is retained. The very short 2.2 ns pulse from the EJ-204 would further require an ultra-fast analysis ASRC. An investigation into alternative scintillators with more favourable gamma/neutron discrimination abilities such as EJ-276, may be advisable. An implemented coded aperture system [59], could also greatly enhance the spatial accuracy of the imaging system and improve its resistance to background radiation, although detrimentally, the overall sensitivity and the field of view is typically reduced. Active electronic collimation techniques have been proposed in the literature as practical alternatives that offer higher signal-to-noise rejection and a wider field of view [60].

8   Conclusions

Within this extensive study, a compact imaging system capable of real-time simultaneous detection and localisation of gamma rays, thermal neutrons and fast neutrons has been investigated both theoretically and experimentally. The three layered imaging system features several scintillating materials including GS10 lithium glass, EJ-204 plastic scintillator and CsI(Tl) inorganic scintillator, in which Compton and neutron scattering techniques are utilised in parallel. Within all of these three layers, an 8x8 silicon photomultiplier array has been used as a compact method of capturing the scintillation protons produced within the detection layers. The 192 signals from the SiPMs are investigated individually, a process which requires a large volume of back end electronics and some high-speed components. Furthermore, algorithms have been produced in order to process the signals produced and produce in real-time a graphical output representing the radiological component of the incident field. Monte Carlo software was used to optimise and verify the design through comparison with experimental results gained subsequently with the instrument using Cs-137 as a gamma ray source and Cf-252 as a neutron and gamma source. Outcomes were that the instrument operates successfully within optimised scenarios – i.e. when single mode sources have been placed a few cm from the instrument. Within these limits, the instrument operates successfully with intrinsic efficiency of typically in the order of 10^{-4} and with spatial resolution of between 5% and 15%.

References

1.   *Detection of radioactive materials at borders* 2002, Radiation Safety Section, International Atomic Energy Agency , Jointly sponsored by IAEA, WCO,EUROPOL and INTERPOL: Vienna, Austria.
2.   Agency, I.A.E., *IAEA Inicdents and Trafficking Database (ITDB) Incidents of nuclear and other radioactive material out of regulatory control*, in *2018 Fact Sheet*. 2018, International Atomic Energy Agency Vienna, Austria.

3. *Safeguards Techniques and Equipment*. 2011, International Atomic Energy Agency, IAEA.

4. Al Hamrashdi, H., S.D. Monk, and D. Cheneler, *Passive Gamma-Ray and Neutron Imaging Systems for National Security and Nuclear Non-Proliferation in Controlled and Uncontrolled Detection Areas: Review of Past and Current Status*. Sensors, 2019. **19**(11): p. 2638.

5. Whitney, C.M., et al., *Gamma-neutron imaging system utilizing pulse shape discrimination with CLYC*. Nuclear Instruments & Methods in Physics Research Section A: Accelerators, Spectrometers, Detectors and Associated Equipment, 2015. **784**: p. 346-351.

6. Gmar, M., et al., *GAMPIX: A new generation of gamma camera*. Nuclear Instruments & Methods in Physics Research Section a-Accelerators Spectrometers Detectors and Associated Equipment, 2011. **652**(1): p. 638-640.

7. Carrel, F., et al. *GAMPIX: A new gamma imaging system for radiological safety and Homeland Security Purposes*. in *2011 IEEE Nuclear Science Symposium Conference Record*. 2011.

8. Amoyal, G., et al., *Metrological characterization of the GAMPIX gamma camera*. Nuclear Instruments and Methods in Physics Research Section A: Accelerators, Spectrometers, Detectors and Associated Equipment, 2019. **944**: p. 162568.

9. Dreyer, J.G., M. T. Burks, and E. L. Hull, *Next generation germanium systems for safeguards applications*. 2014: Lawrence Livermore National Lab.(LLNL), Livermore, CA (United States).

10. Gal, O., et al., *CARTOGAM – a portable gamma camera for remote localisation of radioactive sources in nuclear facilities*. Nuclear Instruments and Methods in Physics Research Section A: Accelerators, Spectrometers, Detectors and Associated Equipment, 2001. **460**(1): p. 138-145.

11. Aryaeinejad, R. and D.F. Spencer, *Pocket dual neutron/gamma radiation detector*. IEEE Transactions on Nuclear Science, 2004. **51**(4): p. 1667-1671.

12. Runkle, R.C., et al., *Lynx: An unattended sensor system for detection of gamma-ray and neutron emissions from special nuclear materials*. Nuclear Instruments and Methods in Physics Research Section A: Accelerators, Spectrometers, Detectors and Associated Equipment, 2009. **598**(3): p. 815-825.

13. Ayaz-Maierhafer, B., et al., *Angular resolution study of a combined gamma-neutron coded aperture imager for standoff detection*. Nuclear Instruments and Methods in Physics Research Section A: Accelerators, Spectrometers, Detectors and Associated Equipment, 2013. **712**: p. 120-125.

14. Soundara-Pandian, L., et al. *CLYC in gamma -Neutron imaging system*. in *IEEE Nuclear Science Symposium Conference Record*. 2012. Honolulu, HI, USA.

15. Enqvist, A., M. Flaska, and S. Pozzi, *Measurement and simulation of neutron/gamma-ray cross-correlation functions from spontaneous fission*. Nuclear Instruments and Methods in Physics Research Section A: Accelerators, Spectrometers, Detectors and Associated Equipment, 2008. **595**(2): p. 426-430.

16. Todd, R.W., Nighting.Jm, and D.B. Everett, *Proposed Gamma Camera*. Nature, 1974. **251**(5471): p. 132-134.

17. Everett, D.B., et al. *Gamma-radiation imaging system based on the Compton effect*. in *Proceedings of the Institution of Electrical Engineers-London*. 1977. IET Digital Library: London, UK.

18. Singh, M. and R.R. Brechner, *Experimental Test-Object Study Of Electronically Collimated SPECT*. Journal of Nuclear Medicine, 1990. **31**(2): p. 178-186.

19. Peterson, S.W., D. Robertson, and J. Polf, *Optimizing a three-stage Compton camera for measuring prompt gamma rays emitted during proton radiotherapy*. Physics in Medicine and Biology, 2010. **55**(22): p. 6841-6856.

20. Du, Y.F., et al., *Evaluation of a Compton scattering camera using 3-D position sensitive CdZnTe detectors*. Nuclear Instruments and Methods in Physics Research, Section A: Accelerators, Spectrometers, Detectors and Associated Equipment, 2001. **457**(1-2): p. 203-211.

21. Polack, J.K., et al. *Dual-particle imager for standoff detection of special nuclear material*. in *2011 IEEE Nuclear Science Symposium Conference Record*. 2011. Valencia, Spain.

22. Poitrasson-Riviere, A., et al., *Dual-particle imaging system based on simultaneous detection of photon and neutron collision events*. Nuclear Instruments & Methods in Physics Research Section a-Accelerators Spectrometers Detectors and Associated Equipment, 2014. **760**: p. 40-45.

23. Al Hamrashdi, H., D. Cheneler, and S.D. Monk, *Material optimization in dual particle detectors by comparing advanced scintillating materials using two Monte Carlo codes*. Nuclear Instruments and Methods in Physics Research Section A: Accelerators, Spectrometers, Detectors and Associated Equipment, 2017. **869**(Supplement C): p. 163-171.

24. H. Al Hamrashdi, S.D.M., D. Cheneler. *Design and Optimisation of a Three Layers Thermal Neutron, Fast Neutron and Gamma-Ray Imaging System*. in *Nuclear instrumentation and measurement methods in nuclear environments*. 2019. EPJ Web of Conferences.

25. Knoll, G.F., *Radiation detection and measurment*. Fourth ed. 2010, New York, NY, USA: John Wiley and Sons.

26. *6-lithium glass bespoke to your application*. [cited 2019 03/12/2019]; Available from: https://scintacor.com/products/6-lithium-glass/.

27. *General Purpose Plastic Scintillators EJ-200, EJ-204, EJ-208, EJ-212*. [cited 2019 25/07/2019]; Available from: https://eljentechnology.com/images/products/data_sheets/EJ-200_EJ-204_EJ-208_EJ-212.pdf.

28. *Csl(Tl) a rugged, non-hygroscopic alternative to NaI*. [cited 25/07/2019; Available from: https://johncaunt.com/materials/csl-tl/.

29. *Stopping-Power & Range Tables for Electrons, Protons, and Helium Ions*. 02/08/2019]; Available from: https://www.nist.gov/pml/stopping-power-range-tables-electrons-protons-and-helium-ions.

30. Bravar, U., et al. *Development of the fast neutron imaging telescope*. in *IEEE Nuclear Science Symposium Conference Record, 2005*. 2005.

31. Mascarenhas, N., et al. *Development of a Neutron Scatter Camera for Fission Neutrons*. in *2006 IEEE Nuclear Science Symposium Conference Record*. 2006.

32. *J-SERIES SIPM: Silicon Photomultiplier Sensors, J-Series (SiPM)*. [cited 2019 15/05/2019]; Available from: https://www.onsemi.com/PowerSolutions/product.do?id=J-SERIES%20SIPM.

33. Spinelli, A. and A.L. Lacaita, *Physics and numerical simulation of single photon avalanche diodes.* IEEE Transactions on Electron Devices, 1997. **44**(11): p. 1931-1943.

34. Turchetta, R., *Analog electronics for radiation detection*. 2016.

35. van Eijk, C.W.E., *Inorganic Scintillators for Thermal Neutron Detection.* Ieee Transactions on Nuclear Science, 2012. **59**(5): p. 2242-2247.

36. *USB-2633 User's Guide*. [cited 2017 05/05/2017]; Available from: https://www.mccdaq.com/pdfs/manuals/USB-2633.pdf.

37. *LMx19 High Speed Dual Comparator*. [cited 2019 23/09/2019]; Available from: http://www.ti.com/lit/ds/symlink/lm319-n.pdf.

38. *mcculw 0.9.7*. Sep 5, 2017 [cited 2018 01/07/2018]; Available from: https://pypi.org/project/mcculw/.

39. Elliott, C., et al., *National Instruments LabVIEW: A Programming Environment for Laboratory Automation and Measurement.* JALA: Journal of the Association for Laboratory Automation, 2007. **12**(1): p. 17-24.

40. *MATLAB and Statistics Toolbox Release 2017b*. The MathWorks, Inc.: Natick, Massachusetts, United States.

41. NEA, O. *Java-based nuclear data information system*. 16/01/2016 [cited 2016 10/02/2016]; Available from: http://www.oecd-nea.org/janis/.

42. Martin, R.C., J.B. Knauer, and P.A. Balo, *Production, distribution and applications of californium-252 neutron sources.* Applied Radiation and Isotopes, 2000. **53**(4): p. 785-792.

43. Billnert, R., et al., *New prompt spectral γ-ray data from the reaction 252Cf(sf) and its implication on present evaluated nuclear data files.* Physical Review C - Nuclear Physics, 2013. **87**(2).

44. Goorley, J.T.J., Michael R.; Booth, Thomas E.; Brown, Forrest, et al., *Initial MCNP6 Release Overview - MCNP6 version 1.0*. 2012.

45. *MCNP6^{TM} User's Manual*. Los Alamos National Laboratory

46. *iM2720 Storm Case*. [cited 2019; Available from: https://peliproducts.co.uk/im2720-storm-case.html?gclid=EAIaIQobChMIis3hyIKF5AIVhbHtCh2olgESEAAYAiAAEgKOyfD_BwE.

47. Ban, G., et al., *Ultracold neutron detection with 6Li-doped glass scintillators.* The European Physical Journal A, 2016. **52**(10): p. 326.

48. Hausladen, P., et al. *Induced-Fission Imaging of Nuclear Material*. in *51 Annual Meeting of the Institute of Nuclear Materials Management*. 2010. United States.

49. Goldsmith, J.E.M., M.D. Gerling, and J.S. Brennan, *A compact neutron scatter camera for field deployment.* Review of Scientific Instruments, 2016. **87**(8).

50. Gamage, K.A.A., M.J. Joyce, and G.C. Taylor, *Investigation of three-dimensional localisation of radioactive sources using a fast organic liquid scintillator detector.* Nuclear Instruments and Methods in Physics Research Section A: Accelerators, Spectrometers, Detectors and Associated Equipment, 2013. **707**: p. 123-126.

51. Brooks, F.D., *A scintillation counter with neutron and gamma-ray discriminators.* Nuclear Instruments and Methods, 1959. **4**(3): p. 151-163.

52. Brooks, F.D., R.W. Pringle, and B.L. Funt, *Pulse Shape Discrimination in a Plastic Scintillator.* IRE Transactions on Nuclear Science, 1960. **NS-7**(2-3): p. 35-38.

53. Owen, R.B., *The Decay Times of Organic Scintillators and Their Application to the Discrimination Between Particles of Differing Specific Ionization.* IRE Transactions on Nuclear Science, 1958. **5**(3): p. 198-201.

54.   Marrone, S., et al., *Pulse shape analysis of liquid scintillators for neutron studies.* Nuclear Instruments and Methods in Physics Research Section A: Accelerators, Spectrometers, Detectors and Associated Equipment, 2002. **490**(1–2): p. 299-307.

55.   D'Mellow, B., et al., *Digital discrimination of neutrons and γ-rays in liquid scintillators using pulse gradient analysis.* Nuclear Instruments and Methods in Physics Research, Section A: Accelerators, Spectrometers, Detectors and Associated Equipment, 2007. **578**(1): p. 191-197.

56.   Aspinall, M.D., et al., *The empirical characterization of organic liquid scintillation detectors by the normalized average of digitized pulse shapes.* Nuclear Instruments and Methods in Physics Research, Section A: Accelerators, Spectrometers, Detectors and Associated Equipment, 2007. **578**(1): p. 261-266.

57.   Liu, G., et al., *A digital method for the discrimination of neutrons and γ rays with organic scintillation detectors using frequency gradient analysis.* IEEE Transactions on Nuclear Science, 2010. **57**(3 PART 3): p. 1682-1691.

58.   Joyce, M.J., et al., *Real-time, digital pulse-shape discrimination in non-hazardous fast liquid scintillation detectors: Prospects for safety and security.* IEEE Transactions on Nuclear Science, 2012. **59**(4 PART 2): p. 1245-1251.

59.   Oda, M., *High-Resolution X-Ray Collimator with Broad Field of View for Astronomical Use.* Applied Optics, 1965. **4**(1): p. 143-143.

60.   Byrd, R.C., et al., *Nuclear detection to prevent or defeat clandestine nuclear attack.* IEEE Sensors Journal, 2005. **5**(4): p. 593-609.